AD_____

GRANT NUMBER: DAMD17-94-J-4511

TITLE: Real-Time 3-D Ultrasonic Diagnostic Imager for
        Battlefield Application

PRINCIPAL INVESTIGATOR: Mr. Timothy White, Mr. Kenneth R. Erikson,
                         Mr. Anthony M. Nicoli

CONTRACTING ORGANIZATION: Loral Infrared and Imaging Systems
                           Lexington, Massachusetts 02173

REPORT DATE: October 1995

TYPE OF REPORT: Annual

PREPARED FOR: U.S. Army Medical Research and Materiel Command
               Fort Detrick, Maryland 21702-5012

DISTRIBUTION STATEMENT: Approved for public release;
                         distribution unlimited

The views, opinions and/or findings contained in this report are
those of the author(s) and should not be construed as an official
Department of the Army position, policy or decision unless so
designated by other documentation.

19960417 159

DTIC QUALITY INSPECTED 3

DISCLAIMER NOTICE

THIS DOCUMENT IS BEST
QUALITY AVAILABLE. THE
COPY FURNISHED TO DTIC
CONTAINED A SIGNIFICANT
NUMBER OF PAGES WHICH DO
NOT REPRODUCE LEGIBLY.

REPORT DOCUMENTATION PAGE

Public reporting burden for this collection of information is estimated to average 1 hour per response, including the time for reviewing instructions, searching existing data sources, gathering and maintaining the data needed, and completing and reviewing the collection of information. Send comments regarding this burden estimate or any other aspect of this collection of information, including suggestions for reducing this burden, to Washington Headquarters Services, Directorate for Information Operations and Reports, 1215 Jefferson Davis Highway, Suite 1204, Arlington, VA 22202-4302, and to the Office of Management and Budget, Paperwork Reduction Project (0704-0188), Washington, DC 20503.

1. AGENCY USE ONLY (*Leave blank*)	2. REPORT DATE October 1995	3. REPORT TYPE AND DATES COVERED Annual--1 Oct 1994-30 Sep 1995

4. TITLE AND SUBTITLE

Real-Time 3-D Ultrasonic Diagnostic Imager for Battlefield Applications

5. FUNDING NUMBERS

DAMD17-94-J-4511

6. AUTHOR(S)

Mr. Timothy White, Mr. Kenneth R. Erikson, Mr. Anthony M. Nicoli

7. PERFORMING ORGANIZATION NAME(S) AND ADDRESS(ES)

Loral Infrared & Imaging Systems
Lexington, Massachusetts 02173

8. PERFORMING ORGANIZATION REPORT NUMBER

9510-23

9. SPONSORING/MONITORING AGENCY NAMES(S) AND ADDRESS(ES)

U.S. Army Medical Research and Materiel Command
Fort Detrick, Maryland 21702-5012

10. SPONSORING/MONITORING AGENCY REPORT NUMBER

11. SUPPLEMENTARY NOTES

The views, opinions, and/or findings contained in this report are those of the authors and should not be construed as an official Department of the Army position, policy, or decision unless so designated by other documentation.

12a. DISTRIBUTION/AVAILABILITY STATEMENT

Approval for public release; distribution unlimited

12a. DISTRIBUTION CODE

13. ABSTRACT *(Maximum 200 words)*

Ultrasound imaging at 5 MHz has been demonstrated with an electronically scanned two-dimensional hybrid array and acoustic lens. A readout integrated circuit (ROIC), originally designed for infrared imaging, was hybridized to a 44x64 element piezoelectric array. The original readout electronics were also modified by adding a range gate. Real-time diffraction limited images of high reflectance targets were obtained with the f/1.0 doublet lens.

This report summarizes the results of Phase I (12 months) of a three-year, two-phase program. Phase I demonstrated a prototype real-time imager using adaptations of existing infrared camera components. Phase II (24 months) will result in a laboratory demonstration prototype ultrasonic imnaging system to prove the clinical utility of this technology.

14. SUBJECT TERMS

Ultrasound, 3D Imaging, 2D Array, Medical Imaging, Portable

15. NUMBER OF PAGES
53

16. PRICE CODE

17. SECURITY CLASSIFICATION OF REPORT Unclassified	18. SECURITY CLASSIFICATION OF THIS PAGE Unclassified	19. SECURITY CLASSIFICATION OF ABSTRACT Unclassified	20. LIMITATION OF ABSTRACT Unlimited

NSN 7540-01-280-5500

Standard Form 298 (Rev. 2-89)
Prescribed by ANSI Std. Z39-18
298-102

FOREWORD

Opinions, interpretations, conclusions and recommendations are those of the author and are not necessarily endorsed by the US Army.

__✓__ Where copyrighted material is quoted, permission has been obtained to use such material.

__✓__ Where material from documents designated for limited distribution is quoted, permission has been obtained to use the material.

__✓__ Citations of commercial organizations and trade names in this report do not constitute an official Department of Army endorsement or approval of the products or services of these organizations.

__NA__ In conducting research using animals, the investigator(s) adhered to the "Guide for the Care and Use of Laboratory Animals," prepared by the Committee on Care and Use of Laboratory Animals of the Institute of Laboratory Resources, National Research Council (NIH Publication No. 86-23, Revised 1985).

__NA__ For the protection of human subjects, the investigator(s) adhered to policies of applicable Federal Law 45 CFR 46.

__NA__ In conducting research utilizing recombinant DNA technology, the investigator(s) adhered to current guidelines promulgated by the National Institutes of Health.

__NA__ In the conduct of research utilizing recombinant DNA, the investigator(s) adhered to the NIH Guidelines for Research Involving Recombinant DNA Molecules.

__NA__ In the conduct of research involving hazardous organisms, the investigator(s) adhered to the CDC-NIH Guide for Biosafety in Microbiological and Biomedical Laboratories.

Timothy E White
_____
PI - Signature   Date

Contents

Figures

Tables

INTRODUCTION

The objective of this program is to apply a solid state, staring, ultrasonic hybrid array to demonstrate the first real-time, portable C-scan diagnostic ultrasound medical imaging system with three-dimensional (3-D) capability for battlefield and trauma care.

Current B-scan ultrasound imaging limits the visualization of 3-D structures because 1-D B-scan arrays only image 2-D slices. These slices must then be reconstructed in the operator's mind to obtain a mental 3-D "picture" of the item of interest. Automatic movement of the transducer with computer reconstruction (off line) has recently been introduced by some manufacturers, but the systems are slower, more costly, and harder to use than conventional B-scan imaging instruments. They are not well suited to battlefield use.

Recognizing the importance of 3-D imaging, the ultrasound industry is in search of a technical solution to building high resolution, 2-D ultrasound arrays. Our solution is unique. It consists of constructing large imaging ultrasound arrays using processes derived from ARPA supported technology for infrared focal plane arrays (IRFPAs). We have directly applied existing designs and processes from thermal imaging systems to prove our ultrasound imaging capability.

This technology bridges the large gap between taking vital signs and making basic observations in the field, and taking CT scans back in a hospital. With C-scan technology brought to the field, deep tissue damage assessment is done quickly, enabling earlier intervention. This is true for either battlefield environments or EMT/ambulance applications. Real-time imagery also affords the opportunity for transmission, remote diagnosis, and archiving of information. This can also benefit health care in remote locations where specialists and expensive imaging diagnostic equipment is not available.

Earlier efforts had already proven the feasibility of the 2-D transducer hybrid array. They had successfully imaged the direct illumination of a focused source with our transducer array technology. We believe this 44 x 64 element ultrasound array to be the largest operating two dimensional (2-D) ultrasound array in existence.

During Phase I of this project, our goal was to demonstrate real-time C-scan imagery from reflecting targets. Our approach was to build 2-D ultrasonic hybrid transducers using a diced array of piezoelectric elements mated to an existing readout integrated circuit (ROIC). We also modified existing hardware to enable the capture and analysis of real time C-scan imagery. To accomplish this, we modified an existing IR camera to provide range gate and timing controls necessary for ultrasonography. While this proved to be an expeditious and cost effective course for the feasibility demonstration, it also had inherent limitations.

In parallel with this effort and in support of the real time imagery Phase I goal, the IRFPA-FM program established a transducer fabrication capability based on the IR read out integrated circuit and infrared focal plane fabrication technology developed from our IR detector fabrication technology base.

This report describes the work performed in Phase I with an emphasis on the key technologies demonstrated, together with the challenges overcome and those identified for Phase II. As described below, the Phase I effort demonstrated the feasibility of an ultrasonic battlefield imager using 2-D hybrids as the ultrasonic transducer by imaging reflected energy from both specular and diffuse scattering targets.

Our Phase II program builds on the success of the initial feasibility components developed in Phase I. We believe our approach will have benefit in locating foreign object fragments; the location and extent of hemorrhage; and in improving techniques for guided surgery and biopsy.

SCIENTIFIC & TECHNICAL MERIT

The goals of our medical ultrasound imaging system development are visualization of the interior of a human subject with:

- Excellent image quality

- Real-time frame rates

- Image manipulation to obtain any derived view or cross-section

- Portability

- Low cost

Demonstration of imaging with a 2816 element ultrasonic hybrid array is a milestone achievement in medical ultrasound.

RELEVANCE TO ARPA

Our imaging ultrasound array is the application of dual use technology derived from ARPA sponsored developments. Arrays are derived from IRFPA technology, using acoustically sensitive materials in place of the IR detectors. Under the recently awarded flexible manufacturing program with ARPA/MTO, Loral has also demonstrated fabrication of ultrasound hybrid arrays. By using the same IR hybrid fabrication line that supplies DoD and commercial IR imaging products, ultrasound arrays have been made available to this program without significant additional startup expenses, providing maximum synergy of ARPA activities.

CAPABILITIES AND COMMERCIALIZATION

We have assembled a team that includes key leaders in diagnostic ultrasound medicine, equipment development, and imaging systems:

- *University of Rochester, Center for Biomedical Ultrasound:* Dr. Kevin Parker, Director. The center is the oldest and largest interdisciplinary research organization in the world devoted to all aspects of medical imaging.

- *Loral Infrared & Imaging Systems (LIRIS):* A leader in military and commercial application of electro-optic imaging technologies, LIRIS will design and fabricate the ultrasonic imaging arrays and associated electronics.

- *Marvin E. Lasser, Inc.:* Pioneer of 3D ultrasound arrays and related signal and image processing.

THE BATTLEFIELD ULTRASONIC DIAGNOSTIC IMAGER (BUDI)

FEASIBILITY DEMONSTRATION SYSTEM DESCRIPTION

The Phase I feasibility demonstration system is a bistatic, staring, ultrasonic imager. It consists of a 5 MHz transmit transducer, a "physical beamformer" or acoustic imaging mirror/lens, a two-dimensional ultrasonic hybrid transducer array, and camera support electronics. These elements are described below.

The 2-D Piezoelectric/ROIC Hybrid Array

Figure 1 is a schematic cross-section of the hybrid array. It consists of a piezoelectric plate that has been partially cut (diced\reticulated) into individual array elements and then bonded (hybridized) electrically and mechanically to a silicon integrated circuit, known as a Read Out Integrated Circuit (ROIC), with indium "bumps".

All the ROICs used in Phase I were designed for an Infrared Camera
that was fabricated eight years ago.

This existing ROIC has 136 x 192 individual elements on 50 μm centers. The 5 MHz (center frequency) piezoelectric array was designed to have 44 x 64 elements on 150 μm centers so that each ultrasonic element is connected in parallel to a 3 x 3 subarray of the ROIC. (Figure 1 is a concept drawing and does not show this 3 x 3 connection). Since the acoustic wavelength in water at 5 MHz is 300 μm, the square array elements are thus $\lambda/2$ on a side.

The total of 2816 active array elements is more than a factor of 20 larger than most high performance commercial ultrasonic systems.

ROIC Operation

A schematic block diagram of the ROIC is shown in Figure 2 together with the horizontal and vertical readout logic which allows an individual array element (Figure 3) to be addressed.

Figure 4 is a block diagram of the entire readout system and Figure 5 describes the operation. Image collection begins with the emission of an ultrasound pulse from the transmitter. A negative range gate pulse is applied to all 2816 elements in parallel through the detector common electrode on the front surface of the piezoelectric material. Its delay is selected to coincide with ultrasonic energy returning from the object plane of interest. Its width is also under user control. For the duration of this pulse, a parasitic diode in the amplifier at each cell acts as a peak detector, storing an entire frame of ultrasound information. This peak detected value is read out element by element into an external transimpedance amplifier after which it is digitized to 8 bits as Frame A. The array is then reset by the reset pulse. This process is repeated without any ultrasound present to form Frame B, which is stored in memory and represents the "fixed pattern" noise, due to different electronic offsets or other noise, on a pixel by pixel basis. Frame A (ultrasound present) is repeated, however, this time the fixed pattern B is subtracted from the values of frame A thus improving signal to noise ratio. The (A-B) frame is then formatted and output to a gray scale monitor as conventional RS-170 video.
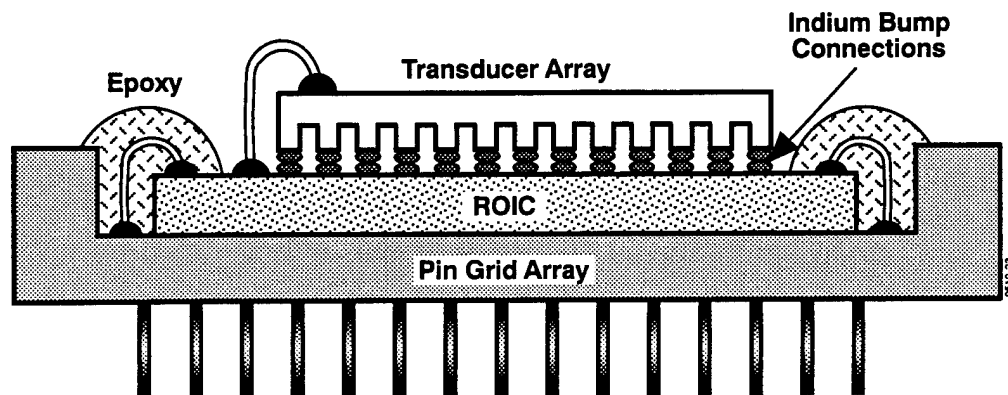
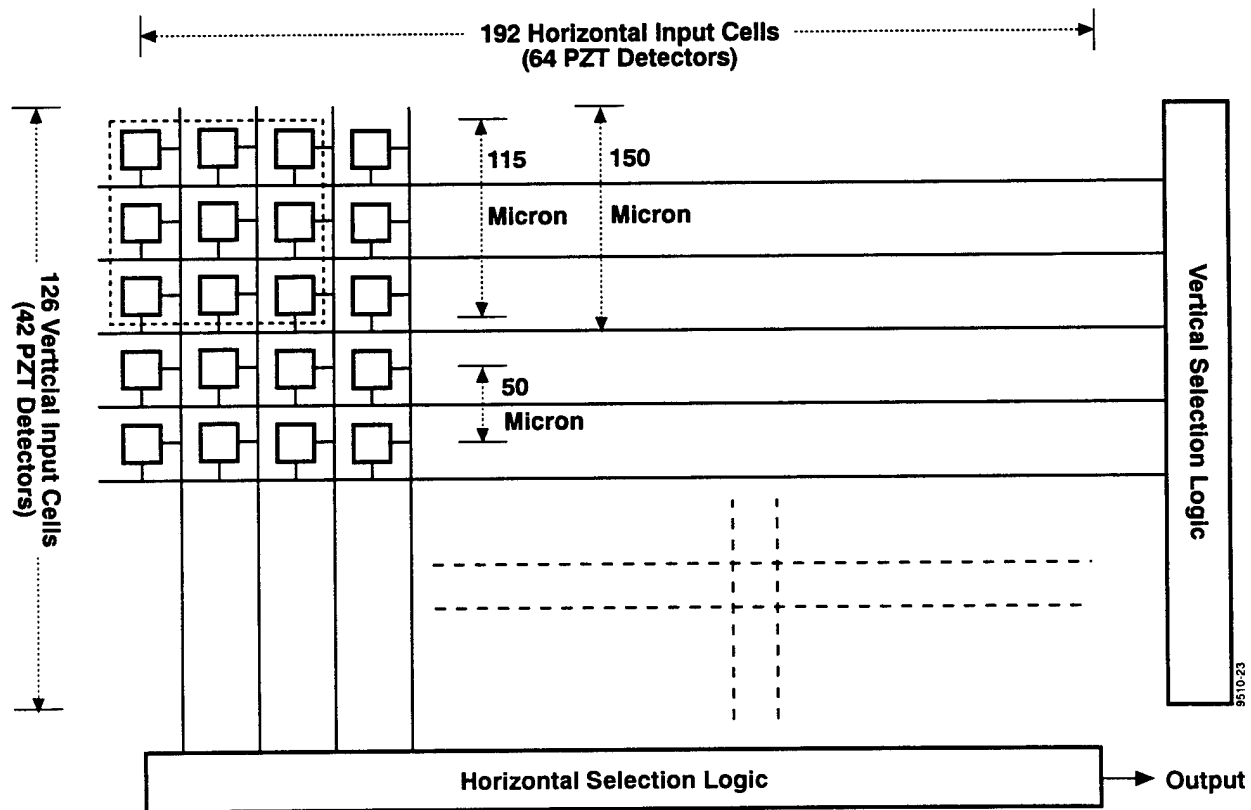**Figure 1. 2D Piezoelectric/ROIC Hybrid Array**

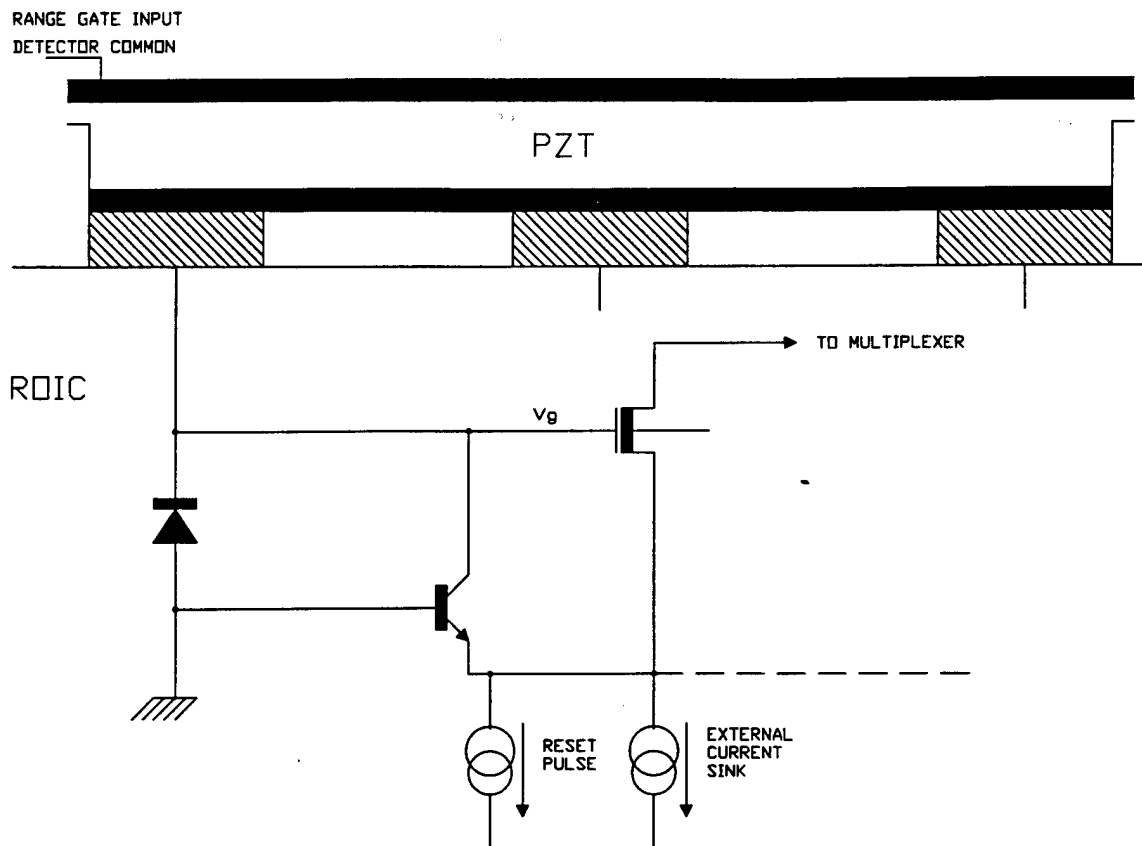**Figure 2. Ultrasound Array Readout IC (ROIC)**

RANGE GATE INPUT
DETECTOR COMMON

PZT

ROIC

TO MULTIPLEXER

Vg

RESET PULSE

EXTERNAL CURRENT SINK

Figure 3. Ultrasound Input Cell

Detector Common

PZT

Range Gate

Peak Detector

Reset

Amp

X-Y Mux

FPA Video Out

FOCAL PLANE ARRAY

FPA Video Out

Fixed Pattern Subtraction

A, B

A, B

8 Bit A/D

Video Formatting (RS-170)

Gray Scale Monitor

Transimpedence Amplifier

B

8 Bit D/A

Digital Memory Frame B
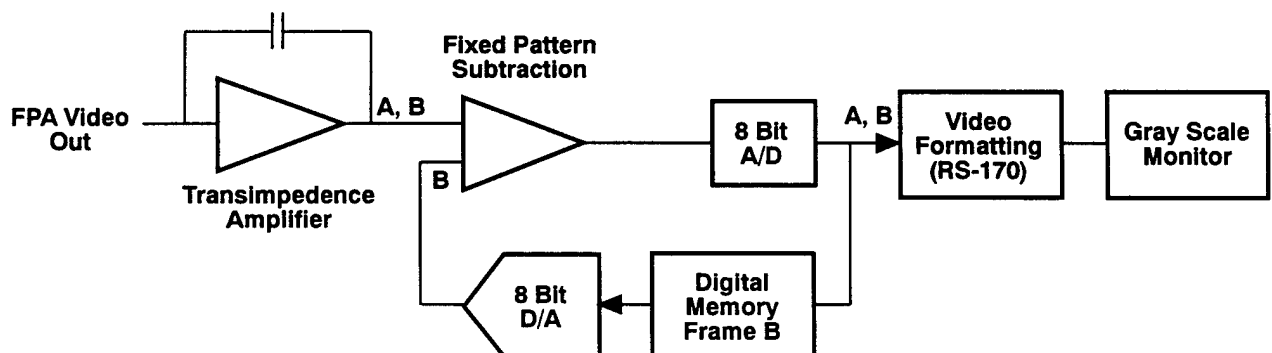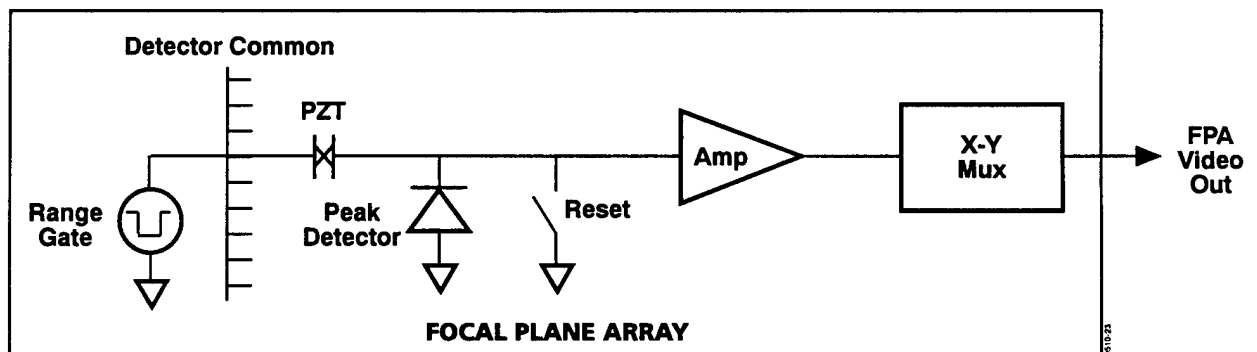
Figure 4. Ultrasound Camera Video Channel Block Diagram

8.33 Milliseconds

Reset Pulse   A   B   A

Range Gate   Tw

Ultrasound Transmit Pulse   Tp

Signal Detector

Sample Return Signal

Vg Signal   Detector Level

Diode Conducts

Inverted Composite Video

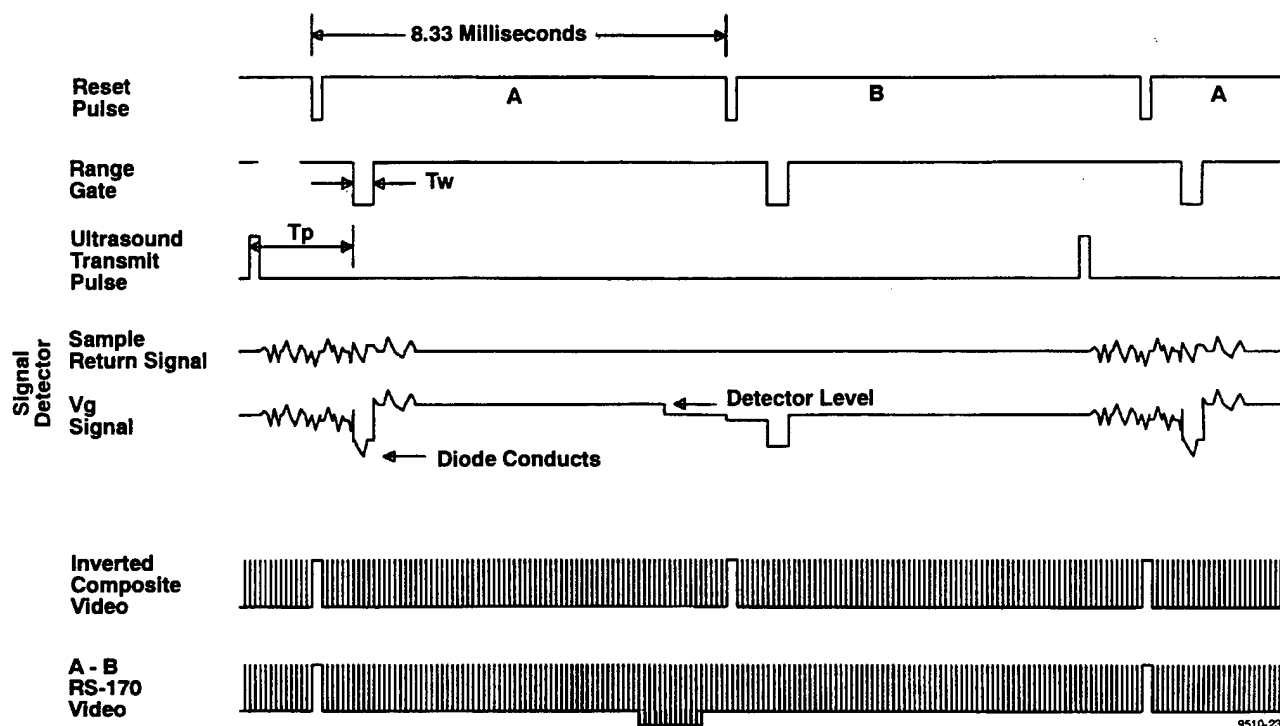A - B RS-170 Video

9510-23

Figure 5. Experimental Ultrasound Camera Response and Timing

PHASE I PROGRESS & ACCOMPLISHMENTS

PIEZOELECTRIC ARRAY FABRICATION

The piezoelectric array was fabricated from a wafer of PZT-5A using a conventional semiconductor dicing saw and conventional processes. As shown in Figure 6A, the first arrays were "partially reticulated", i.e. the saw cuts were penetrated into the PZT 250 μm (66%) leaving a substantial amount of material at the front (acoustic port) of the array. The saw kerf is about 38 μm and the aspect ratio of the cuts is 6.6:1. In these first arrays, the saw kerf was left unfilled. Thirty (30) partially reticulated arrays were fabricated. Experiments disclosed a relatively high level of interelement mechanical crosstalk, which is presumed to be caused by the partial reticulation.

Process development was begun to produce a "fully reticulated" array as shown in Figure 6B. The piezoelectric material available for this work had a two layer matching section bonded to the front face. Attempts were made to dice completely through the PZT into the magnesium layer in two directions, however, the dicing operation caused failure in the PZT/magnesium bond resulting in loss of array elements and this approach was abandoned.

"Fully reticulated" arrays were produced with the structure shown in Figure 6C. In this case the PZT was sawed in one direction, backfilled with epoxy, then sawed at right angles and backfilled a second time. Finally, a silver epoxy electrode/matching layer was applied. Five fully reticulated arrays have been fabricated. Bowing of the array, presumably caused by shrinkage of the silver epoxy layer has been a significant problem, since the flatness required for reliable hybridization is ±5 μm. Figure 7 is an SEM image of a piezoelectric array.
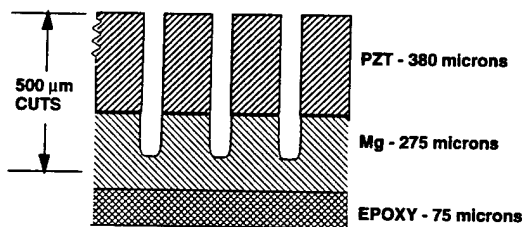
PARTIALLY RETICULATED TRANSDUCER ARRAY
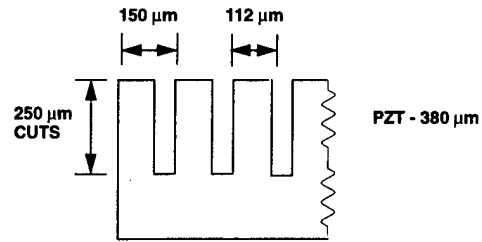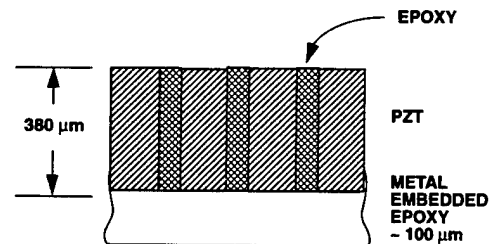

A

ORIGINAL

FULLY RETICULATED TRANSDUCER

B

ATTEMPT

C

PRESENT STATUS

Figure 6. Transducer Array Configurations

Experimental results with these arrays, although limited, have confirmed that the crosstalk is substantially reduced with the fully reticulated structure.

HYBRIDIZATION

The hybridization process (Figure 8) consists of metal bumps onto the back side of the array using proprietary IRFPA techniques. The array and the ROIC (with matching indium bumps) are then aligned with a specialized optical probe (Figure 8A), the probe is removed (Figure 8B) and the two parts are pressed together under a prescribed force/time profile. There is no heat involved in the cold welding process.

The completed hybrid is mounted in a conventional integrated circuit (PGA) package and the ROIC is wire bonded to the pins in a conventional manner (Figure 1).

CAMERA DESCRIPTION

As part of the work in Phase I, four cameras were modified to add the range gate function and timing controls. Additional modifications were made to improve dynamic range and sensitivity.

Details of camera performance are shown in Table 1. The measurements were made with the same hybrid array and experimental arrangement by changing the drive voltage with a step-switched attenuator. The ultrasound beam was reflected from a large planar reflector which was imaged by the lens. The minimum signal levels are relative numbers for intercomparison of the cameras only.

Table 1. Camera Performance

	Camera			
	1	2	3	4
Dynamic Range - dB	18	28	20	28
Minimum Signal - dB	-33	-43	-35	-43

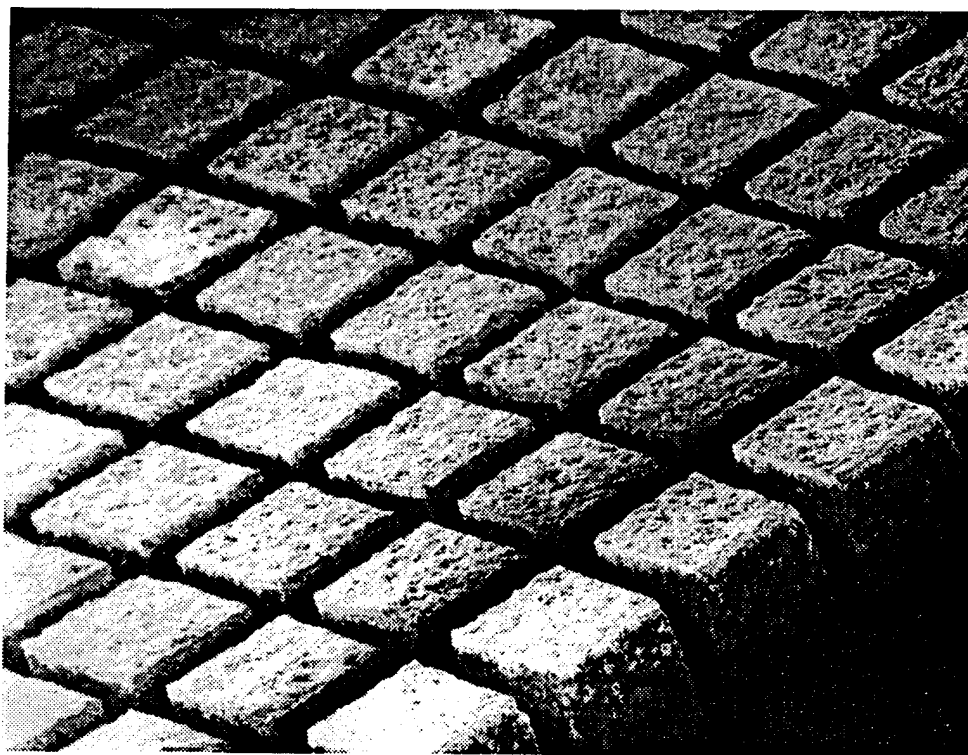Figure 7. SEM Image of Piezoelectric Array

```
A                                          B
```
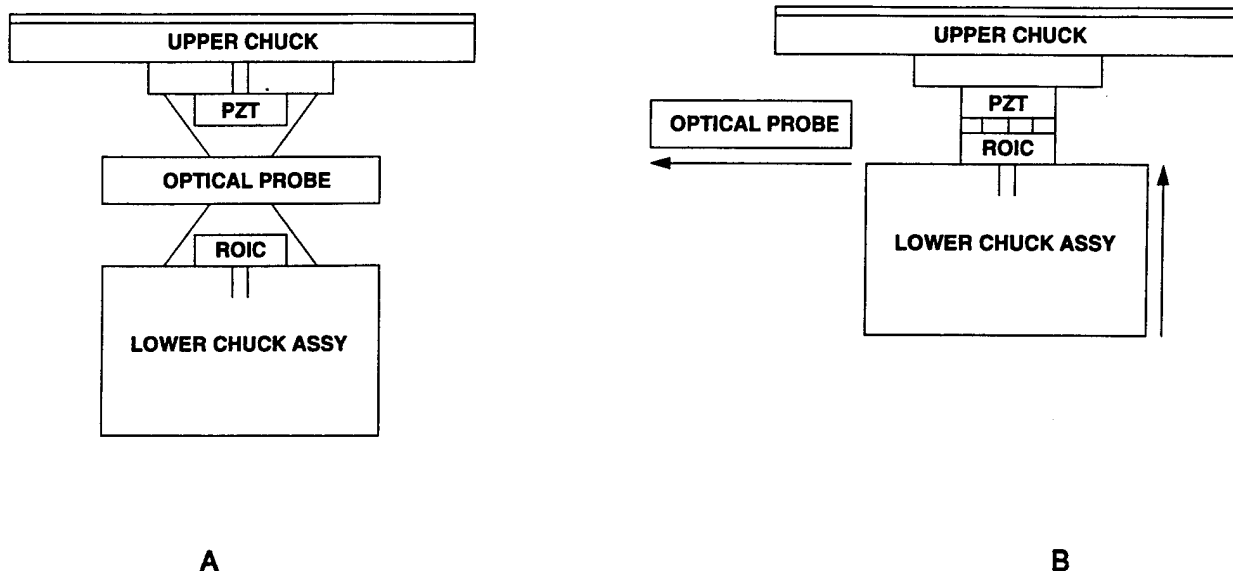
Figure 8. Hybridization Process

IMAGING EXPERIMENTS

Parallel Approaches to Physical Beamforming

Two parallel "physical beamforming" approaches to imaging were associated with the Phase I program: an acoustical mirror-based (reflective) system and a multi-element acoustic lens (refractive) system.

A schematic drawing of the mirror-based system is shown in Figure 9. A spherical cap (virtual point source) transmitter is arranged to insonify a volume such as the body through a membrane. Returning echoes from a narrow region in the object are imaged by the ultrasound mirror onto a piezo-electric receiver array, which is controlled by the ROIC. After processing, the acoustic information is converted to video and displayed on a conventional gray scale monitor.

Figure 10 is a schematic drawing of the lens-based system. This feasibility system is immersed in a water tank and also uses a separate, but collimated transmitter. Returning echoes are imaged with a two element acoustic lens onto a receiver array and read out as in the mirror based system.

Reflective Imaging System

The reflective imaging system work was discontinued after initial testing. While the concept has some attractive features, this particular implementation of a reflective imager suffered from a number of limitations:

1. Due to the obscuration of the receiver array, a single mirror imaging system must be operated off-axis which substantially increases image aberrations.

2. The mirror offers only a single optical surface for correction of aberrations.

3. The mirror is too small for high spatial resolution. It should be f/1.0 or faster.

4. Diffraction from the receiver array in the middle of the ultrasonic field, the mirror and support and the rubber membrane support dominated the image.

5. Isolation of the receiver array from the water medium was attempted through a latex condom which presented practical difficulties in working with the arrays themselves as well as an uncontrolled variable in the acoustical path.
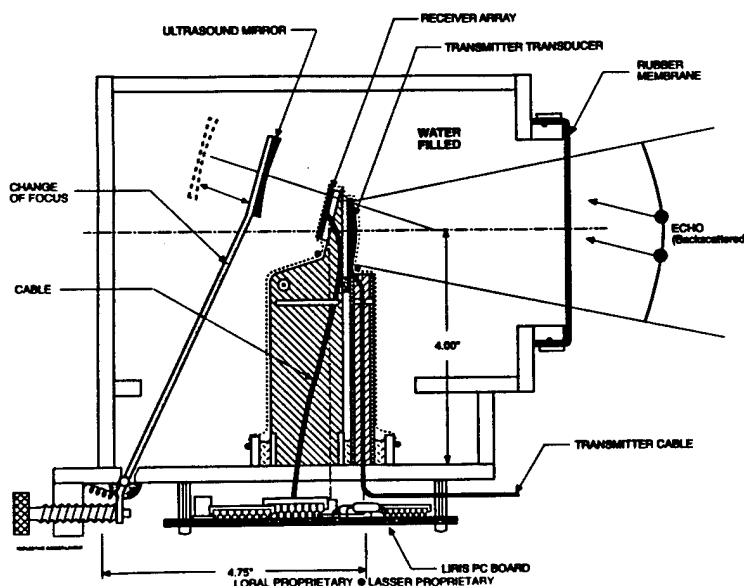
- Imager operational
- High crosstalk observed in image
- Awaiting fully reticulated array in LCC package

Figure 9. Reflective Imager Setup

WATER TANK WALL ⟶

Ultrasonic Lens

Transmitter

ARRAY STAGE

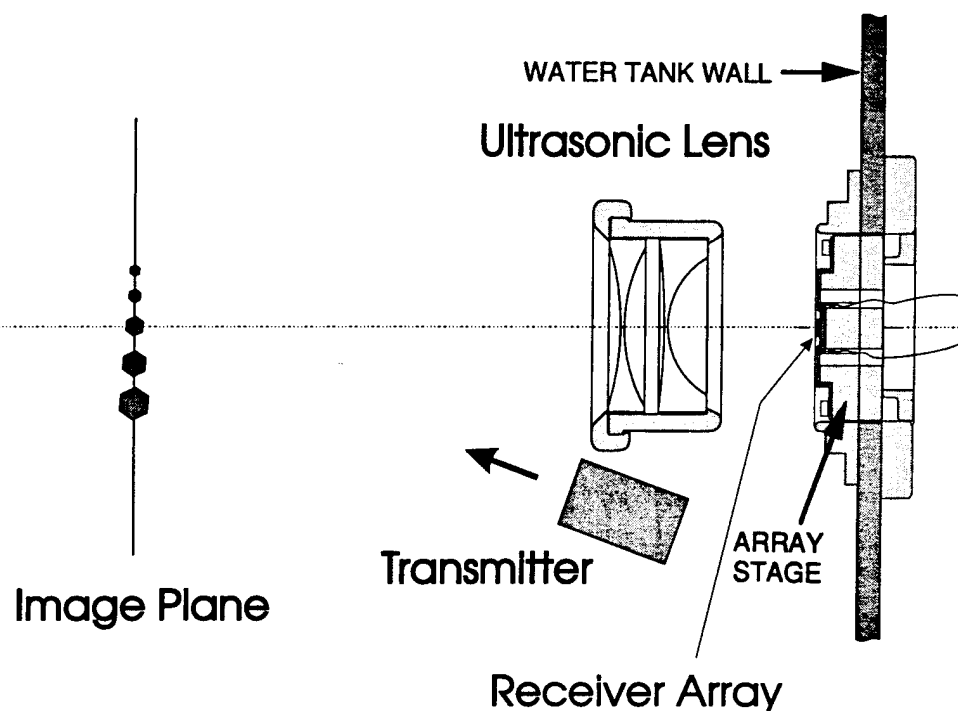## Image Plane

Receiver Array

Figure 10. Refractive Imaging Setup

Refractive Imaging System

The refractive imaging system was designed to be a laboratory feasibility system which requires objects to be immersed in a water tank for imaging.
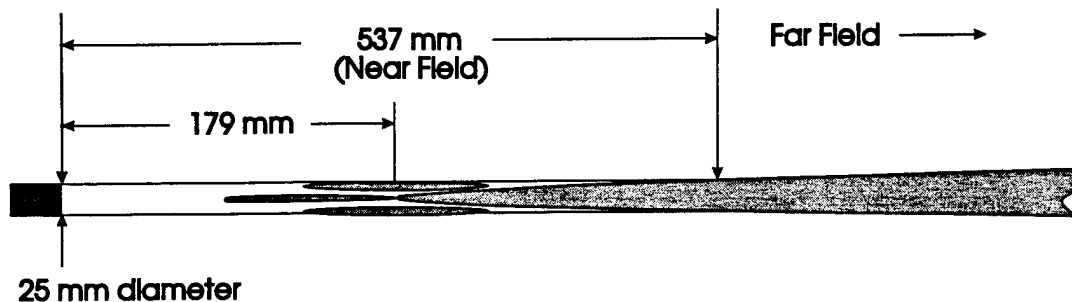
Transmitter

The transmitter is a 5 MHz, 25 mm diameter, unfocused, commercial off-the-shelf, piston radiator. The unfocused sound beam, (shown in Figure 11 as a CW or continuous wave) is collimated from the face of the transducer to approximately 500 mm. In actual operation the transmitter was pulsed.

Ultrasonic Lens

The ultrasonic doublet lens was designed using standard optical lens design computer software in routine use at LIRIS. A ray trace and predicted performance parameters of the uncoated f/1.0 polystyrene lens is shown in Figure 12. The "as designed" 85% diffraction blur circle diameter numbers refer to object space and also include aberrations. Two of the four surfaces of the lens are aspherical.

The lens was machined using a numerically controlled lathe to a nominal tolerance of 50 μm (or 1/6 ultrasound wavelength). Measurement of the lens surfaces with a depth gage accurate to ± 1 μm disclosed that three of the four surfaces were within 5 μm of the design value. The fourth surface, one of the aspherical surfaces proved to be approximately 50 μm from the design value; however, it was within the stated machining tolerance. The "as built" numbers in Figure 12 reflect this change in actual lens shape. These performance differences are probably unmeasurable in the water tank.

Figure 11. Transmit Beam Profile — 5 MHz-25 mm Diameter

Focal Length = 50 mm, f/# = 1.0
Depth of Field = 1 mm
Minification 3:1
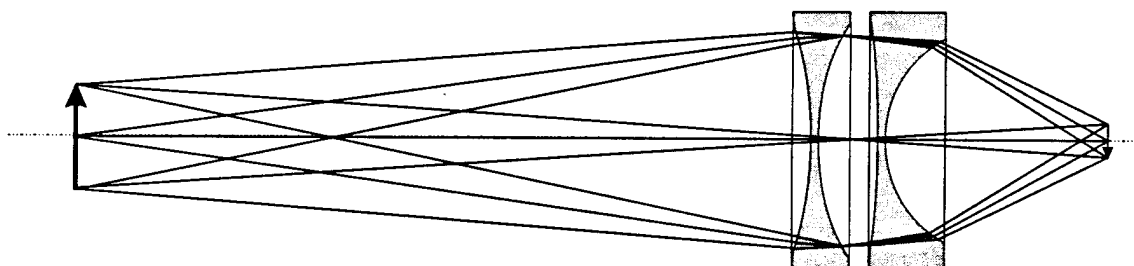
FRACTIONAL OBJECT HEIGHT	85% ENCIRCLED DIFFRACTION BLUR (mm)	
	AS DESIGNED	AS BUILT
0	0.91	0.92
0.5	0.87	0.89
1.0	0.94	0.96

Figure 12. Ultrasonic Doublet Lens

Shear Waves re Image Quality

One of the questions posed at the technical review of 31 May 1995 was the influence of shear waves formed in the acoustic lens due to mode conversion of the compressional (longitudinal) at the water/lens interface. Although shear waves do not propagate in water, they can be generated at the water/lens interface, propagate across the solid material of the lens and be mode converted back into compressional waves in the water at the lens/water interface. This spurious wave might then be detected at the array and would create an unfocused artifactual signal, limiting contrast.

Figure 13 is a ray trace of such an image using the shear wave index of refraction in polystyrene of 0.95. The shear wave velocity of sound in polystyrene is fortunately very close to that of the surrounding water medium. The lens thus has almost no "power", i.e. rays pass through essentially undeviated. Another way to express this is that the lens is essentially a piece of "invisible" material as far as shear waves are concerned.

Since the lens has almost no power, any shear waves that might be generated are spread out across the lens aperture. From the ratio of the areas, the array thus intercepts at most about 1% of any shear wave energy developed.

A/R Coatings

Reflection of compressional waves at the lens/water interface is a more serious issue. Figure 14 is a graph of the reflection from a polystyrene water interface as a function of incident angle. At normal (0 degrees) incidence, the reflection coefficient is 24.7% at each interface, which is rather large. (Uncoated optical glass typically has 8% reflection at an air interface.) The answer, as in optical lenses, is anti-reflection coating. The reflection coefficient of a simple single quarter wave coating is also shown in Figure 14. It can be seen that even out to an incident angle of 30 degrees, this simple layer is an improvement over an uncoated lens. This simple coating has less than 1% reflection out to about 10 degrees. Figure 15 is a graph of the frequency response of such a coating at normal incidence. A 2 MHz bandwidth can be achieved rather easily.

Some limited initial testing was done with one A/R coating material that appeared very promising. It was not successful, however, due to an error in the vendors literature for the elastic modulus of the coating. A/R coatings will be one of the key areas for development in Phase II.

Transducer Hybrid Interface

Figure 16 is a schematic drawing of the hybrid array stage with the mounted PGA package shown partially cut away. This stage mounts the hybrid array to the water tank as shown in Figure 10. The PGA package is located in the plastic stage on four edges and the backside and is held in place by metal clips, one of which is shown in the figure. The wires from the PGA socket are led out through the rear of the stage.

The stage itself is mounted in a fixture attached to and penetrating the side wall of the water tank (Figure 10). A stretched membrane mounted on one side of this fixture contains the water in the tank and allows the array to be acoustically coupled to the water with a drop of oil. This arrangement has proven to be very convenient and repeatable for testing various arrays.

Display and Recording

The acoustical image is displayed on a black and white monitor without any additional image processing at this time. A 3/4 inch VCR was used for recording images.

Shear Wave Index of Refraction = 0.95

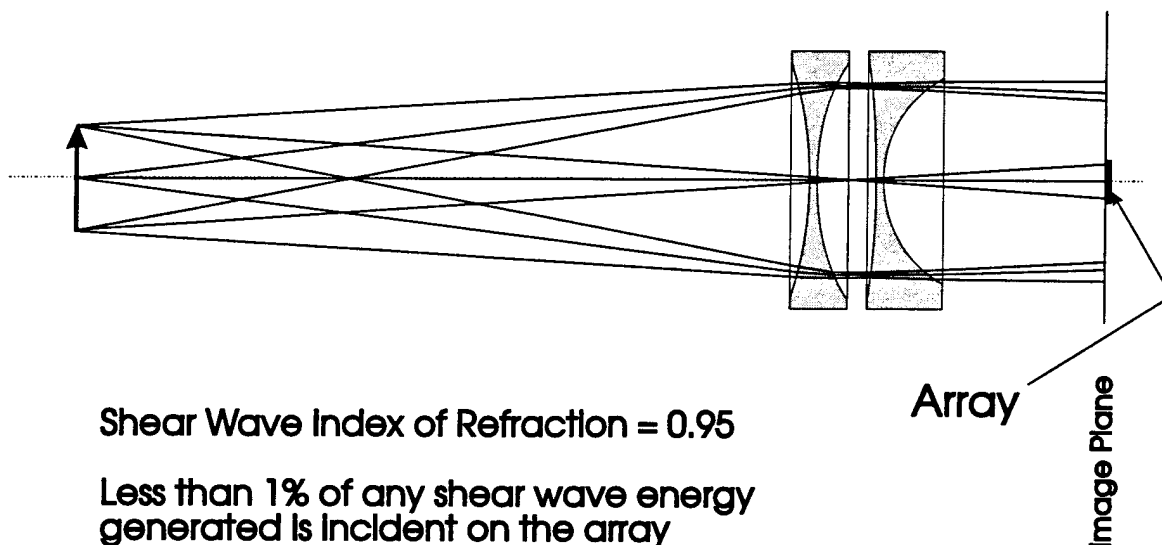Less than 1% of any shear wave energy
generated is incident on the array

Figure 13. Ultrasonic Doublet Lens — Shear Wave "Image" is out of Focus
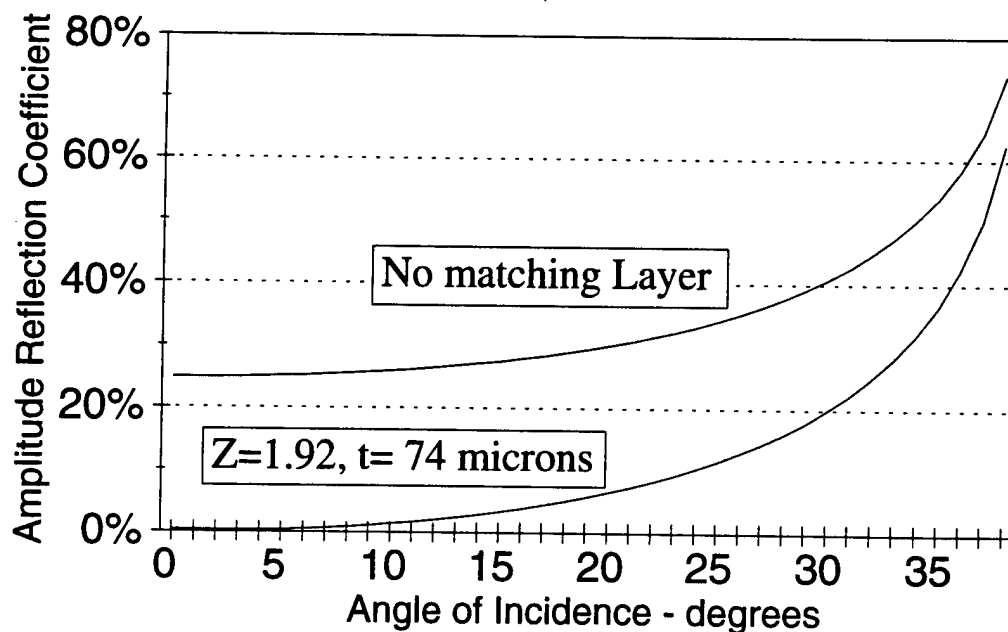

Figure 14. Matching Layer - Quarter Wave — Water to Polystyrene vs Angle
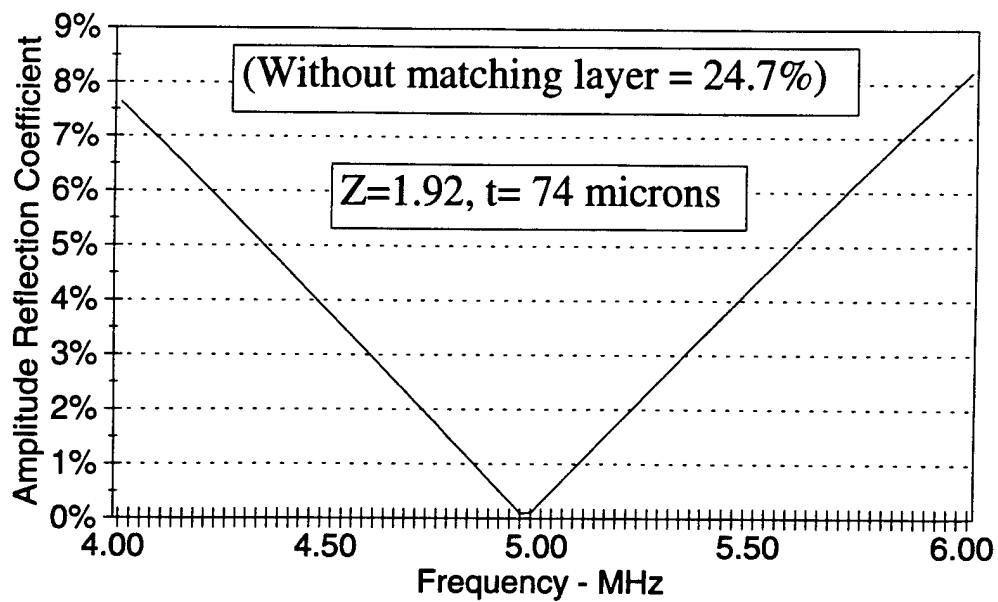
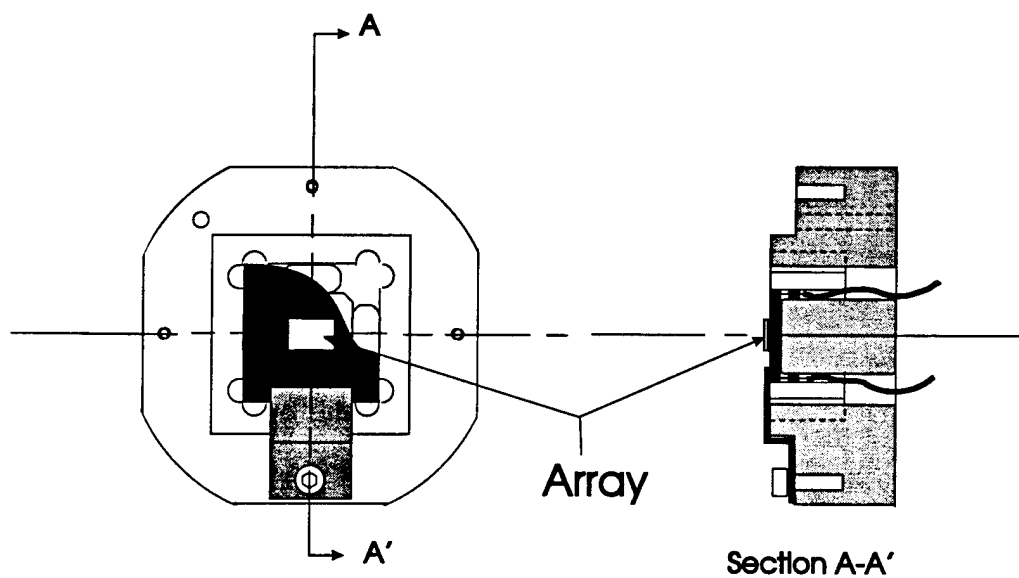**Figure 15. Quarter Wave Matching Layer — Water to Polystyrene/Normal Incidence**

Figure 16. Array Stage (Showing Mounted PGA Package Partially Cut Away)

Predicted Performance of the Refractive Imager

Figure 17 is an idealized graph describing the ultrasonic signal and noise levels in the human body as a function of target depth from the skin surface. It is based on the average value of attenuation in the body of 1 dB/cm/MHz. At 5 MHz, the attenuation is thus 5 dB/cm. The graph is referenced to 0 dB which is the reflection from a perfect reflector.

A perfect reflector at the skin surface thus gives a signal level of 0 dB. If this same reflector is located at a target depth of 2 cm, the signal level is reduced by 20 dB (4 cm total travel distance x 5 dB/cm). At 4 cm, this value is -40 dB, etc.

Targets of interest in the body are generally not perfect reflectors, but have some lower reflectance. Typically large specular reflections such as the boundaries between fat and muscle are -20 dB re a perfect reflector. Non-specular targets such as blood vessels, tumors, small foreign bodies, tissue parenchyma, blood, fluid filled cysts, etc. range in scattering power from nearly in the specular range to extremely small values depending on their size and orientation. In the absence of blood vessels, cartilage and connecting tissue, a large relatively uniform tissue such as liver parenchyma is generally considered to be a "volumetric" scatterer, i.e., it is composed of a statistical ensemble of unresolved scatterers.

Echo levels in the body at one depth cover a wide amplitude range, for example, 40 dB. Any imaging system attempting to image from the skin to deep inside the body at 5 MHz, thus must contend with a huge dynamic range on the order of 100 dB.
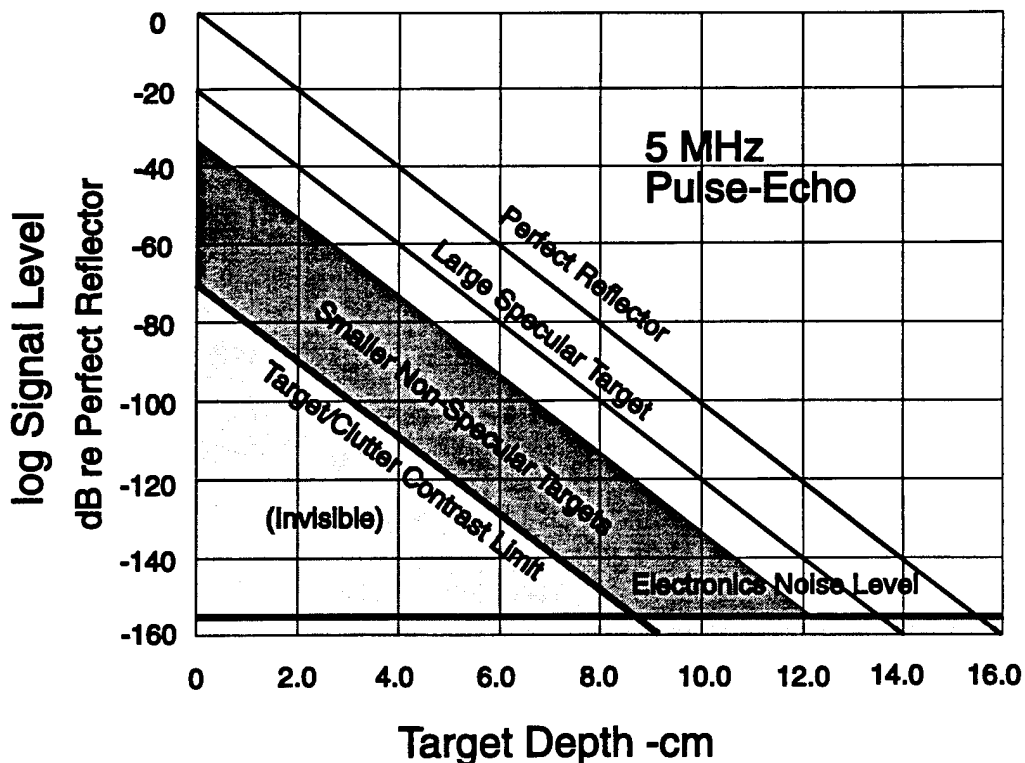

Figure 17. Signal and Noise Levels in the Body

There are two limits to the ability of the imaging system to detect small targets. The first is the electronic noise level as shown in Figure 17. Clearly, with ordinary techniques, signals lower in amplitude than this noise level will not be seen at any depth. The electronics noise limit is generally the limiting factor at a certain depth (beyond 8 cm in Figure 17). Targets with larger scattering power, however, can be seen out to greater depths (almost 14 cm in this example).

Increasing the input acoustic levels can boost echo signals above the electronics noise level and make it possible to image deeper. Practical limits in the transmitter, presumed safety limits and/or governmental regulatory limits do not permit acoustic input levels to the human body to be raised beyond a certain point.

The other limit is the target clutter/contrast ratio. This limit is determined both by the imaging system itself and the scattering properties of the tissue. This is a topic of great contemporary interest and research in the medical ultrasound field, where it is often discussed in terms of aberration correction. Unlike the case of the electronic noise level limit, it is not possible to increase the input acoustic level to improve target contrast ratio because it is essentially constant - independent of input levels. Note that the target contrast ratio applies to any kind of beamforming, including "physical" beamformers such as lenses or mirrors as well as electronic beamforming.

Reference 1, entitled "Scattering from a Multiple Random Phase Screen Model of a Random Inhomogeneous Medium", by Bernard Steinberg of the University of Pennsylvania, is a reprint of a relevant research paper. It is included as the Attachment to this report. Quoting from this reference:

> "Wavefronts distort when ultrasound propagates through an inhomogeneous medium, lowering target contrast in the image and introducing image artifacts. Isotropic scattering reduces the contrast...
>
> "The paper presents a theory of the effect of scattering upon important image quality parameters such as target to clutter power ratio (TCR) and lateral resolution. Several elements of the theory are tested against experimental data.
>
> "The main findings are:
>
> • When target strength is stronger than background scattering, the principal scattering mechanism is primary (i.e. simple, single or nonmultiple) scattering.
>
> • Scattering produces a halo in the image centered on each scatter source or target. Its width is the order of 2-6 deg at 3 MHz and *(its angular extent)* is proportional to wavelength. (italicized comment added)
>
> • TCR within the halo is linear with 2-D array area, inversely proportional to time delay variance per unit distance and propagation length and decreases as the square of the frequency and correlation distance. The formula is:

$$\mathrm{TCR} = \frac{L^2}{D\omega^2 (\pi \cdot \chi_{0m})^2 (\sigma_{\tau m}^2 / D_m)}$$ (Eq. 1)

where L = array size

D = propagation path length or tissue thickness

ω = $2\pi f$ is the angular frequency

$\pi \cdot \chi_{0m} \approx a$ - typical scatterer size

$\sigma^2_{\tau m}$ = time delay variance

D_m = tissue thickness in which $\sigma^2_{\tau m}$ is measured

"Target dynamic range is about an order of magnitude smaller than TCR...

"The numerator parameter and first two denominator parameters are design parameters. The next two denominator parameters are measured properties of the tissue. The last is the length of the tissue sample in which tissue parameter measurements are made. Thus, time delay variance and correlation distance are the primary tissue measurements required for prediction of TCR in a purely scattering medium.

"The lateral resolution was found to remain λ/L, the width of the diffraction pattern, and unaffected by the scatter field so long as the scattered energy does not obscure the main image lobe."

Refractive Imager Performance

Images

Figure 18 is an image of a set of different size Allen wrenches in a plastic holder taken with one of the cameras and a partially reticulated array. The wrench sizes and spacing between them are shown in Table 2.

Figure 18. Ultrasonic Image of Allen Wrench Set

Table 2. Allen Wrench Set Dimensions

Nominal Size	Width of Face (mm)	Spacing Between Faces (mm)
9/64	2.0	3.9
1/8	1.8	3.8
7/64	1.6	3.5
3/32	1.3	3.4
5/64	1.1	3.2
1/16	0.9	3.0
0.05	0.7	

The wrenches were rotated in the image plane for maximum image brightness and present large specular targets.

The field of view is approximately 25 mm which is consistent with the diameter of the transmitter transducer beam width. The wrenches are all completely and easily resolved. Spatial resolution is thus substantially better than 3 mm and as scaled from the photograph is estimated to be about 1 mm, which corresponds to the theoretical predictions of Figure 12.

An image of the backbone of a formalin fixed mouse, made at the University of Rochester, is shown in Figure 19. The ossifications of the vertebral bodies have relatively large scattering cross-sections.
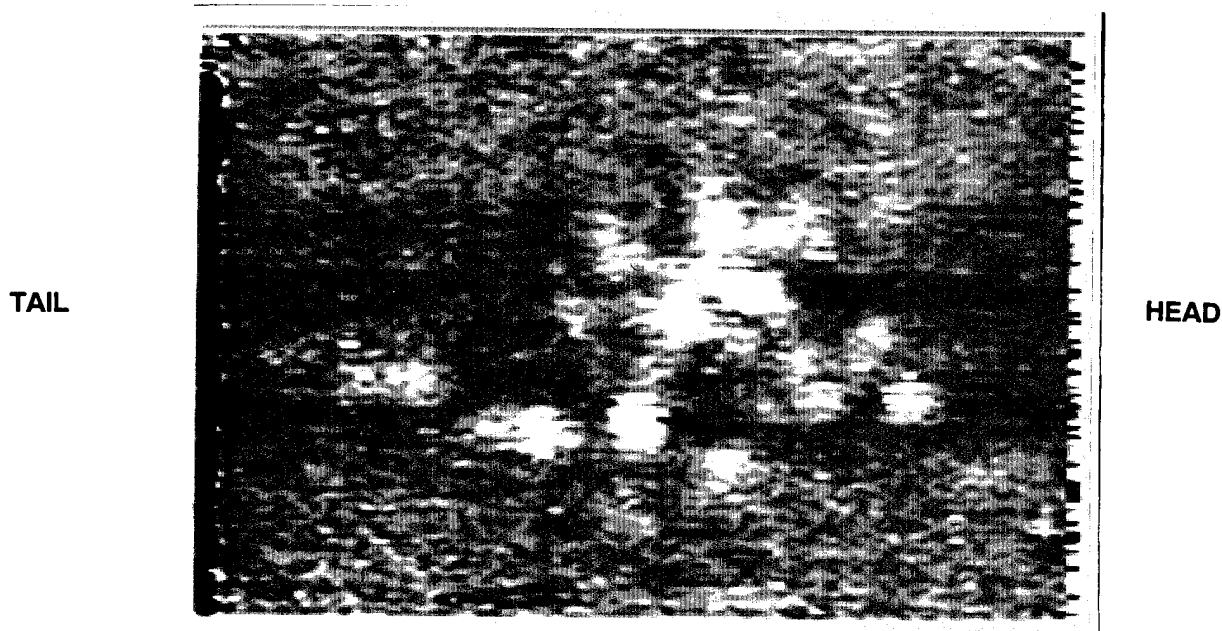
TAIL

HEAD

Figure 19. The Backbone of a Formalin Fixed Mouse

Quantitative Array/Camera Sensitivity and Minimum Detectable Signal

Figure 20 shows the camera sensitivity and minimum detectable signal (noise level) used for these images superimposed on the graph of Figure 17. With the limited sensitivity and dynamic range of this camera, it is clear that only large targets close to the surface or with no intervening tissue can be imaged.

After the technical review of 25 September 1995, camera dynamic range and minimum detectable signal level were substantially improved. Figure 21 is an ultrasonic image of parallel nylon monofilament line targets in a tissue equivalent test object (Model 539, ATS Laboratories, Bridgeport, CT). These line targets are 0.12±5% mm in diameter. They are spaced in 5 mm increments. The target in the center of the image in Figure 21 is 7 mm below the surface of the test object.

Since these line targets are less than $\lambda/2$ in diameter, they are cylindrically isotropic scatterers. Their image is thus the line spread function of the image system. From the 5 mm target spacing, a line width of approximately 1 mm may be observed.

While it is gratifying to see these images and the recent improvements, several points must be raised regarding system sensitivity, dynamic range, and electronic noise levels:

1. Array sensitivity is relatively poor. This is due to many factors:

   a. The tank membrane coupling the front face of the array to the water has not been optimized.

   b. The acoustical properties of the array, including the matching layer(s), mounting, backing, saw-cut fill material, etc. have not been optimized.

   c. The indium bump mounting of the ROIC to the array is not optimized.

   d. The ROIC itself was designed for pyroelectric IR detection, not ultrasound.

2. Camera noise levels are relatively high

   a. Electronic noise is the primary limitation to detection of the low level ultrasound signals from tissue or the tissue equivalent test object. There are many different sources:

   Fixed pattern noise. Array elements are not present or not electrically connected.

   Oscillations. Low frequency, flicker oscillations in the image are a cosmetic defect.

   b. Vibration noise. The piezoelectric array has response at low frequencies which leads to sensitivity to vibration from fans, motors, etc. Use of a vibration isolated optical bench has ameliorated this problem.

   c. Artifacts. There are various artifacts in the video image.

3. Dynamic range is still limited to about 28 dB best case

The first arrays were only partially reticulated (partially diced through) producing relatively high levels of cross talk in the array. Later arrays with complete reticulation appear to have much improved isolation, however, they suffered from other defects due to bowing of the ceramic/silver epoxy matching layer.

(assuming theoretical array transducer sensitivity)
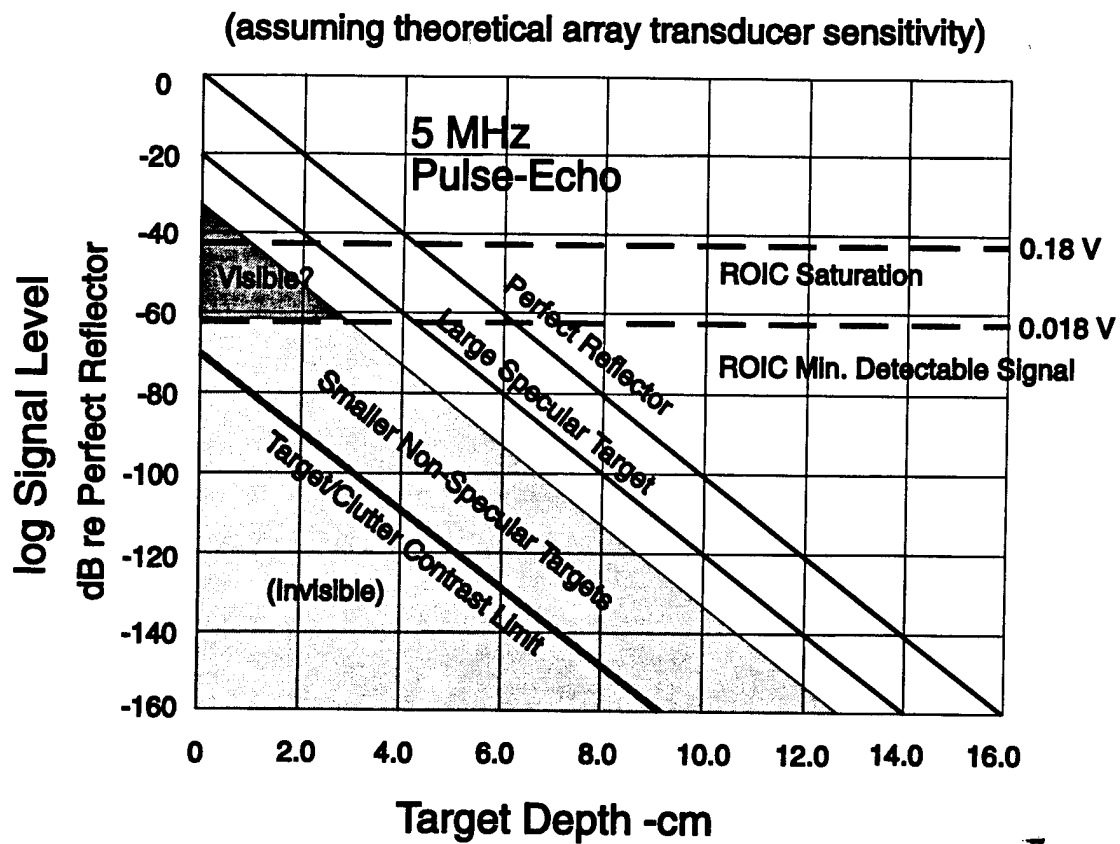
Figure 20. Signal and Noise Levels in the Body — Phase I ROIC
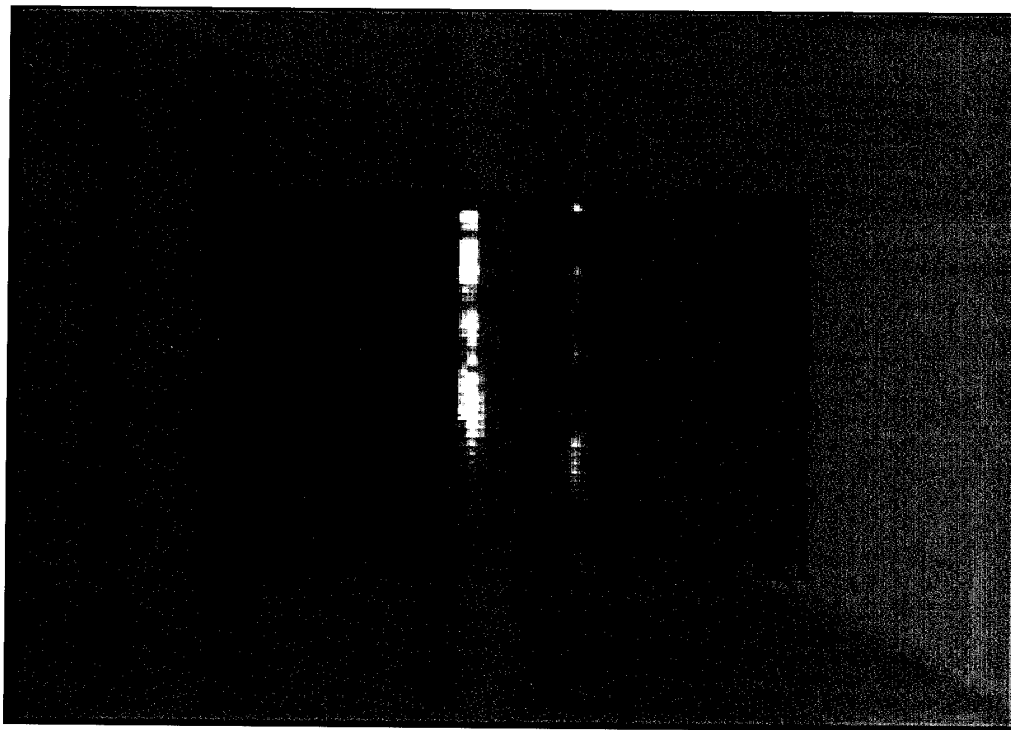
Figure 21. Image of Monofilament Nylon in Test Object
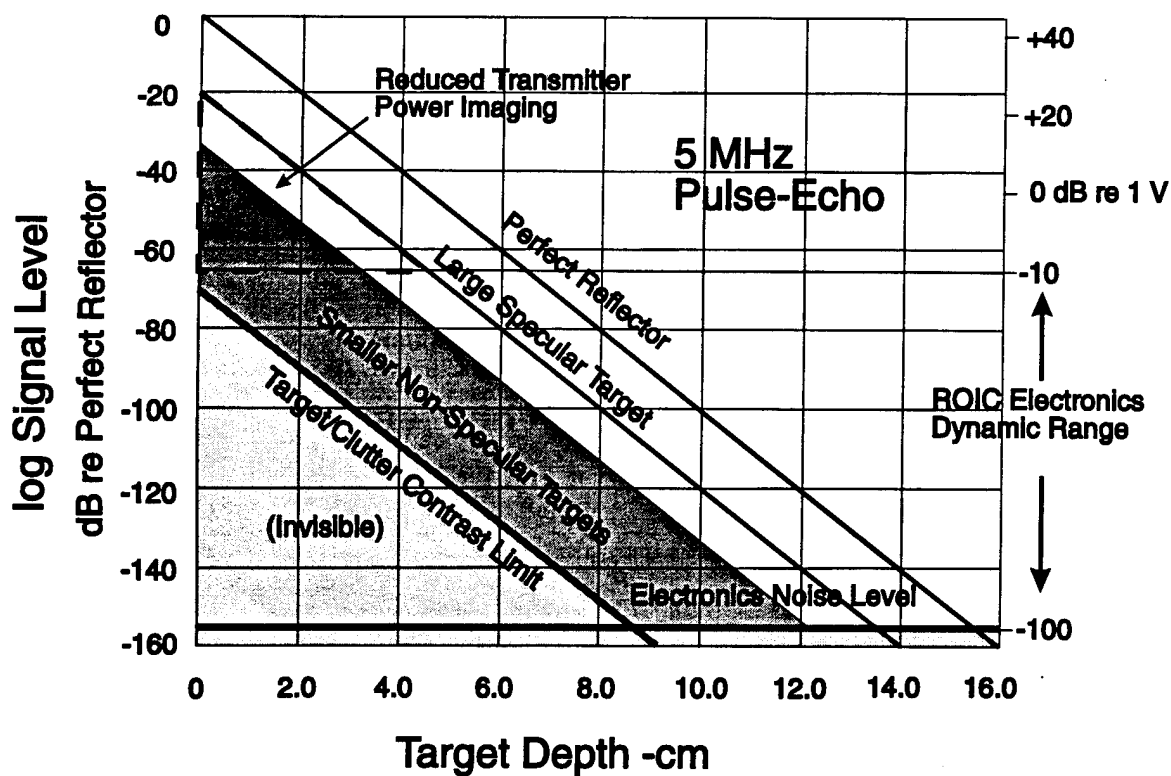
Figure 22. Signal and Noise Levels in the Body — Phase II Electronics

Further improvements in signal to noise ratio together with larger ultrasonic input levels will be required for imaging in the body. This will be achieved by designing an ROIC specifically for the ultrasound system with suitable performance (Figure 22). Little or no additional effort will be expended to further improve the existing IR ROIC or the camera electronics.

CONCLUSIONS

Phase I Accomplishments

Phase I of this effort demonstrated the feasibility of an ultrasonic imager employing two-dimensional hybrid transducers. Significant demonstration included the fabrication of two-dimensional piezoelectric arrays of up to 44x66 elements; the electrical interconnection of these arrays to silicon readout integrated circuits; the fabrication of an acoustic lens; and the imaging of specular and diffuse scattering targets. Images collected to date include specular reflections off metal bar targets, diffuse reflections off monofilament nylon embedded in tissue simulating material, and the backbone of a formalin fixed mouse. The system collects and presents these images in real-time (30 Hz frame rate), and presently resolves targets of ~1 mm at a distance of 200 mm.

OPPORTUNITIES AND CHALLENGES IDENTIFIED

Anti-Reflection Coatings for the Ultrasonic Lens

Anti-reflection coatings for the ultrasonic lens are an important part of the development work in Phase II. Polystyrene remains the material of choice for the lenses because it has a very usable index of refraction, relatively low ultrasonic attenuation and an acoustic impedance close to that of water. It is expected that only a single quarter wave matching layer will be required on each surface. Selection, fabrication and performance verification of this layer will be a high priority for the early part of Phase II work.

Electronics Noise

The ROIC's and cameras used in Phase I were intended for a different application and compromised the result that were achieved. During Phase II, these components will be specifically redesigned to exhibit the low noise levels required for the ultrasound imaging application The design, fabrication and integration of integrated circuits and sensors is the key technology strength of LIRIS.

Target Contrast Ratio Optimization

In the Phase I final review of 25 September 1995, the issue of target contrast ratio was discussed. While it is clear that this is a limiting factor in the performance of any ultrasonic imaging system, quantifying this parameter for an ultrasonic lens based system is another critical task in the early part of Phase II. Methods for optimizing this parameter such as apodization and other signal processing will also be examined.

The results of this work will be compared with contemporary electronic beam forming methods.

ATTACHMENT

"Scattering from a Multiple Random Phase Screen Model of a Random Inhomogeneous Medium"

SCATTERING FROM A MULTIPLE RANDOM PHASE SCREEN MODEL
OF A RANDOM INHOMOGENEOUS MEDIUM*

Bernard D. Steinberg
Valley Forge Research Center
The Moore School of Electrical Engeineering
University of Pennsylvania
Philadelphia PA 19014
steinber@pender.ee.upenn.edu

ABSTRACT

The decrease in image target contrast due to scattering of ultrasound energy by an inhomogeneous body is calculated and tested. The analysis is in terms of measurable parameters of the medium (thickness, phase or time-delay variance and correlation length) and parameters of the scanning equipment (frequency and array size). The propagation medium is modeled as a sequence of thin, random phase screens and the number of screens is related to the sample thickness and to the size of the scattering bodies.

It is found that (1) scattering produces a halo, centered on each target, with diameter (2-6° at 3 MHz) proportional to wavelength, (2) target contrast within the halo, defined as target to clutter power ratio (TCR), increases linearly with 2-D array area, is inversely proportional to tissue sample thickness and time delay variance per unit distance in the tissue and decreases quadratically with correlation distance and frequency and (3) multiple scattering plays no significant role.

Several elements of the theory are tested against experimental data. Although the amount of relevant data is small, the theory checks well against what does exist.

PACS numbers: 43.80.Cs, 43.80.Ev, 43.80.Vj

GLOSSARY OF TERMS

L	array size
λ, f, $\omega = 2\pi f$	wavelength, frequency, angular frequency
λ/L	lateral resolution
σ_ϕ^2	phase variance per screen

σ_τ^2	time delay variance per screen
x_0	e^{-1} correlation distance of tissue
$\Delta u_s = \lambda/\pi x_0$	half-power width of the scatter spectrum:
$a \approx \pi x_0$	typical scatterer size
TCR	target to clutter power ratio within halo
TDR	target dynamic range within halo
D	propagation path length or tissue thickness
$N \approx D/a$	number of screens
$\sigma_{\phi m}^2, \sigma_{\tau m}^2$	measured phase, time delay variance in tissue
D_m	tissue thickness in which $\sigma_{\phi m}^2$ or $\sigma_{\tau m}^2$ are measured

INTRODUCTION

Wavefronts distort when ultrasound propagates through an inhomogeneous medium, lowering target contrast in the image and introducing image artifacts[1-9]. Isotropic scattering reduces the contrast. The artifacts are discrete multipath arrivals that look like targets[9]. The motivation for most studies of this topic is aberration correction for large aperture, 2-D high resolution imaging. This paper deals with isotropic scattering only. Discrete multipath will be dealt with later. The paper presents a theory of the effect of scattering upon important image quality parameters such as target to clutter power ratio (TCR) and lateral resolution. Several elements of the theory are tested against experimental data.

The main findings are:

○ When target strength is stronger than background scattering, the principal scattering mechanism is primary (i.e., simple, single or nonmultiple) scattering.

○ Scattering produces a halo in the image centered on each scatter source or target. It's width is the order of 2-6 deg at 3 MHz and is proportional to wavelength.

○ TCR within the halo is linear with 2-D array area, inversely proportional to time delay variance per unit distance and propagation path length and decreases as the square of the frequency and correlation distance. The formula is $\text{TCR} \approx \dfrac{L^2}{D\omega^2(\pi x_{0m})^2(\sigma_{\tau m}^2/D_m)}$.

○ Target dynamic range is about an order of magnitude smaller than TCR.

§1 models the inhomogeneous medium as a cascade of thin, random phase screens and the incident radiation from the target as a plane wave. In §2 the scattered power P_{scat} per screen

is calculated as a function of the phase variance per screen, and also the ratio of P_{scat} to the power P_{pw} of the emergent plane wave. We also calculate the angular width of the scatter field. From these we determine the TCR in the target image and how the lateral and contrast resolution or target dynamic range are affected by the scatter. The target is the source of the plane wave and the clutter is the scatter or background energy. In §3 we calculate the effective number of screens making up a large body and show how to combine the multiple scattering effects between the many screens. We then calculate the quantities above for the entire propagation medium. §4 discusses related topics. Summary and Observations is §5.

1. THE MODEL

When a point target or source is imaged through a weakly scattering medium (small scattering coefficient) the scattered energy creates a background field that clusters about the target image and decreases its contrast with the background and therefore its visibility. It is the same phenomenon that produces the halo around stars and the ring around the moon that one often sees on humid nights. The ultrasound halo is found to be about 2-6 deg wide at 3 MHz centered about the target. Its effect is minimal with small transducers whose beams are comparable to or larger than the halo. But with narrow beamwidth, high resolution arrays the scattered energy can materially reduce target contrast. The calculations use only measurable or known quantities. The scattered energy is variously called scatter or clutter. The diminution in TCR in the image is calculated as well as the angular width of the scatter field and the effects upon lateral and contrast resolution (or target dynamic range) of the imaging system. The procedure divides the medium into thin slices, calculates the relevant statistical properties per slice and then recombines the slices.

A unit amplitude plane wave from an impulsive source propagates from the left in the positive z direction through a random inhomogeneous medium, defined by a uniform, isotropic distribution of scatterers, located in the x,z plane (Figure 1a)[†] . Each slice is treated as a thin, random phase screen with independent scattering occurring in each screen. Each screen is infinite in length (x axis). Its thickness (z axis) is the order of the scale of the compressibility and density variations of the medium, denoted a in the paper. Each screen is defined by a zero-mean, Gaussian random phase shift process $\phi(x,z)$ with phase variance σ_ϕ^2. $\phi(x,z)$ is the phase delay at frequency f within the signal spectrum through a thin vertical slice perpendicular to the direction of propagation. The propagation delay $\tau(x,z)$ is related to the phase delay by $\phi(x,z) = \omega\tau(x,z)$, $\omega = 2\pi f$. The variation in $\tau(x,z)$ may be attributed to the local medium peturbations, as modeled in the phase screen detail of Figure 1b. The scale of the perturbations is denoted a.

[†] Although the analysis is based upon a plane wave source, the results are also applicable in the focal plane of a focused system close to the focal point. See §4.1.

The time delay variance per slice $\sigma_t^2 = \sigma_\phi^2/\omega^2$. The correlation function of the phase $R(x) = \sigma_\phi^2 \rho(x)$ is modeled as an exponential with correlation distance x_0. x_0 is related to scatterer size a by $a = \pi x_0$ (§2.5).

Tissue parameters σ_ϕ^2 and x_0 are obtained from measured data. x_0 is the value of x for which $\rho = e^{-1}$. Measurements of variations of arrival time across wavefronts disclose σ_ϕ^2. Measurements are usually made through tissue thickness $D > a$, $\Rightarrow$ number of slices $N > 1$. The phase variance through N slices is $\sigma_{\phi,N}^2$ and the relation to the single-slice variance is $\sigma_{\phi,N}^2 = N\sigma_\phi^2$ because of the assumed independence of the phase from screen to screen (§3.5). The measured value of x_0 is not a first-order function of N.

2. SCATTERING FROM A RANDOM PHASE SCREEN

The far-field radiation $f(u)$ from a single, infinite screen (Figure 1b) contains an emergent plane wave $f_{pw}(u)$ plus the scattered field $f_{scat}(u)$. The plane wave is reduced in amplitude to account for the energy in the scattered wave as it passes through the screen. $f(u)$ is the Fourier transform of $\phi(x)$, in units of the reduced angular variable $u=\sin\theta$:

$$f(u) = \int e^{j\phi(x)} e^{jkxu}\, dx$$
$$= f_{pw}(u) + f_{scat}(u) \tag{1}$$

$k = 2\pi/\lambda$ is the wavenumber and $\phi(x)$ is the random phase shift previously described. $f(u)$ is decomposed into the sum of a plane wave $f_{pw}(u) = A\delta(u)$ emerging from the screen and a scattered wave $f_{scat}(u)$. The amplitude of the plane wave is A.

2.1 The emergent plane wave

To calculate $f_{pw}(u)$, $f(u)$ is expanded in a power series and its expectation $E[\circ]$ taken.

$$f(u) = \int (1 + j\phi - \phi^2/2 - j\phi^3/3! + \phi^4/4! \cdots)\, e^{jkxu}\, dx \tag{2}$$

The first term is the incident plane wave. The remainder are the scattered terms. Their mean values (expectations, spatial dc) add (subtract) coherently to (from) the incident plane wave and the total establishes the amplitude A of the emergent plane wave. Thus

$$f_{pw}(u) = Ef(u) = \int (1 + E[j\phi - \phi^2/2 - j\phi^3/3! + \phi^4/4! \cdots])\, e^{jkxu}\, dx = \int A e^{jkxu}\, dx \tag{3}$$

$$A = 1 + E[j\phi - \phi^2/2 - j\phi^3/3! + \phi^4/4! \cdots]$$
$$= 1 + E[\Sigma_{n=1}\, j^n \phi^n/n!]$$
$$= 1 - \sigma_\phi^2/2! + 3\sigma_\phi^4/4! - 5\circ3\sigma_\phi^6/6! + 7\circ5\circ3\sigma_\phi^8/8!.... \tag{4}$$

because the assumed pdf is Gaussian (all odd moments are zero).

The power P_{pw} in the emergent plane wave is proportional to A^2. Ignoring the proportionality factor, $P_{pw} = A^2$ is plotted in Figure 2 (small circles) for a range of values of $\sigma_\phi{}^2$.

2.2 Energy in the scattered field

No loss to absorption is yet included in the model[††]. (When loss is included (§3.6), the conclusions are found to be unaltered.) Consequently the energy in the scattered field $P_{scat} = 1 - A^2$, which is plotted (as stars) in Figure 2, is the difference between the incident (unit) power and P_{pw}. Lastly, the ratio P_{scat}/P_{pw}, is plotted as plus signs. The fields have equal energies at $\sigma_\phi^2 = 0.7$ and the ratio rises to 1.7 at $\sigma_\phi^2 = 1$. Large values of σ_ϕ^2 severely degrade the quality of ultrasound images. From the theory of radiation pattern distortion caused by random phase errors[#, 11] σ_ϕ^2 must fall in the neighborhood of 10^{-2} or less for reasonably acceptable beam quality. Thus practical interest lies to the extreme left of Figure 2, which implies a very weak scattering process in which most of the energy passes through each screen unscattered.

2.3 Angular width of the scattered field

The scattered field is the difference between (2) and (3):

$$
\begin{aligned}
f_{scat}(u) &= \int [j(\phi - E\phi) - (\phi^2 - E\phi^2)/2 - j(\phi^3 - E\phi^3)/3! + (\phi^4 - E\phi^4)/4! \cdots)] \, e^{jkxu} \, dx \\
&= \int [\Sigma_{n=1} \, j^n(\phi^n - E\phi^n) \, /n!] \, e^{jkxu} \, dx \\
&= \int [1 - A + \Sigma_{n=1} \, j^n\phi^n/n!] \, e^{jkxu} \, dx
\end{aligned}
\tag{5}
$$

$f_{scat}(u)$ is a function of the random process $\phi(x)$ and therefore is also a random process. Its power $P_{scat} = 1 - A^2$. Its angular width is found from its angular power density spectrum $S(u)$. $S(u)$ is proportional to the expectation of the square magnitude of the scattered field, $E|f_{scat}(u)|^2$, which in turn can be obtained from the Fourier transform $F\{\circ\}$ of the correlation function calculated from the measured radiation field, i.e., $S(u) = F\{R(x)\}$.

Wavefront correlation experiments performed in *in vivo* breast[12] have measured the normalized correlation function $\rho(x) = R(x)/R(0)$. From these data the correlation function is found to approximate a decaying exponential (Figure 3). Hence we model

---

[††] Absorption is added later in §3.6, where it is found that its inclusion does not materially alter the conclusions of §2.2.

[#] Average sidelobe powerlevel relative to main lobe = ASL = σ_ϕ^2/N_e where N_e is the no. of array elements[11]. Specifying –40 dB for the required ASL and assuming the order of 100 array elements, $\sigma_\phi^2 \approx 10^{-2}$. This formula has been checked repeatedly in adaptive beamforming experiments in radar beginning in the early 1980s[16].

$$\rho(x) = \exp(-x/x_0) \qquad (6)$$

and call x_0 the e^{-1} correlation distance[##]. $x_0 = 1.8$, 3.3 and 3.3 mm for average correlation curves of three groups of asymptomatic women: premenopausal dense breasts, premenopausal fatty and postmenopausal. The number of correlation functions averaged were 35, 52 and 76. Other reported measurements are in the same neighborhood[6,10]. The Figure 3 curves and the body of data from which they come[12] were obtained over long, 12-cm paths, which corresponds to many correlation distances or several phase screens (§3.1). Hence it is possible that the correlation evidence leading to (6) is not representative of a single screen. This is checked in §3.5 where it is shown that the angular spectral width estimated from these data and (6) is representative of a single screen. The result indicates that single scattering dominates, which means that the total scattering spectrum observed out of each of the phase screens approximates a first-order spectrum. This further implies that correlation measurements made from any thickness of tissue disclose x_0.

Based on (6) the unnormalized correlation function and the angular power spectrum are

$$R(x) \approx \sigma_\phi^2 \exp(-x/x_0) \qquad (7)$$

$$S(u) \approx \frac{\sigma_\phi^2 x_0}{1 + (kux_0)^2} \qquad (8)$$

and the half-power width of the scatter power spectrum is

$$\Delta u \approx 2/kx_0 \approx \lambda/\pi x_0 \qquad (9)$$

which, for a frequency of 3 MHz ($\lambda = 0.5$ mm) and for the values of x_0 given above for the mean correlation functions of premenopausal-dense and premenopausal-fatty/postmenopausal breasts, is 0.089 and 0.048 rad or 2.7 and 5.1 deg. Allowing about one standard deviation additional spreads about the means the predicted halo width Δu increases to 2-6 deg at 3 MHz and is inversely proportional to frequency.

2.4 Estimate from breast samples

An independent prediction of halo width can be made from the size of subcutaneous fat globules in breast tissue. Fat globules have random sizes, orientations and radii of curvature.

[##] As distinct from the FWHM measure of correlation distance. The relation between the two for the exponential correlation model (6) is $x_{FWHM} = 1.38 x_0$.

The scale is predominantly in the 5 to 15 mm range. Each globule is a likely candidate for scattering of ultrasound waves, as seen in a radiologist's schematic of a breast section (Figure 4)[13].

Referring back to Figure 1b, the distance between scatterers or density hills shown there is nominally a. Scattered energy from subcutaneous fat should lie largely in the Fourier angular interval $\Delta u_F \approx \lambda/a$, $5 < a < 15$ mm, which at 3 MHz is 0.033-0.1 rad or 1.9 to 5.7 deg. The fact that this interval is substantially identical to the calculated halo width of 2-6 deg from correlation data (§2.3) suggests that subcutaneous fat is one of the contributors to the scattered field.

2.5 Exponential coefficient vs. frequency

Time delay variations should be independent of frequency because they result directly from local tissue density variations. Frequency dependence manifests itself in the phase variance where $\sigma_\phi^2 = \omega^2 \sigma_\tau^2$. Consequently, the phase variance should grow as the square of the frequency. Theory also predicts that x_0 and the scatterer size a are related by $a = \pi x_0$ by equating the two calculations of scatter spectrum width, $\Delta u \approx \lambda/\pi x_0$ (9) and $\Delta u_F \approx \lambda/a$ (§2.4). But a is independent of frequency. Therefore the correlation function should be independent of frequency, which agrees with the 3 and 4 MHz comparison shown in Figure 3.

2.6 Point source image

When the composite field $f(u) = f_{pw}(u) + f_{scat}(u)$ is imaged, whether by spherical lens or transducer (Figure 5), the image (in one dimension) in the focal plane contains the point source and the apparent source distribution of the scattered field, each convolved with the diffraction pattern of the lens or transducer. The target is reduced in amplitude to A and it images as the diffraction pattern of the transducer, with half-power width λ/L. The angular clutter spectrum is depicted in the figure as a continuum, which is not a realistic portrayal because it is a Fourier transform of the random phase-perturbation process $\phi(x)$; hence it too is a random process with peaks and valleys. No instantaneous sample function is so smooth. For simplicity the clutter amplitude spectrum is drawn as a smooth function, which may be interpreted as the sq. rt. of the angular clutter power spectrum S(u). The half-power width is $\lambda/\pi x_0$. The clutter power is $1-A^2$. After convolution with the transducer diffraction pattern the half-power width of the clutter spectrum equals the rms sum of $\lambda/\pi x_0$ and λ/L:

$$\Delta u_s = [(\lambda/\pi x_0)^2 + (\lambda/L)^2]^{1/2} = \lambda/\pi x_0 \oplus \lambda/L \qquad (10)$$

Figure 6 pictures other images. Part a is the image without the phase screen. The unit-amplitude plane-wave image is spread to the diffraction pattern. It consists of a main lobe of

width λ/L plus sidelobes. L is the size of the aperture. The image with the screen is part b; it is the same as the image in Figure 5. Its width is $\approx \lambda/\pi x_0$ for high resolution imaging, for then $L >> \pi x_0$. It is also possible for the opposite condition to hold, i.e., $\pi x_0 > L$, which occurs when the nominal scatterer size exceeds the aperture size of the imaging system. In this case the "scatterer" is a "large" surface (relative to the transducer) such as a wedge which refracts the incident wave and bends the beam. The image is then displaced from its original orientation (in the u-axis) by the refraction angle u_r. Part c depicts the case of wedge refraction plus weak scattering. A realistic "wedge" would have rounded rather than planar facets which would change the focal length of the beam and therefore defocus the image (d). For the pure scattering problem addressed in this paper we ignore refraction and select $\Delta u_s \approx \lambda/\pi x_0$.

2.7 Resolution

It is evident that lateral resolution is unaffected by the scatter field; it remains the width λ/L of the mainlobe of the diffraction pattern of the aperture *unless the scattered energy obscures the main image lobe*[14]. When this happens lateral resolution and contrast vanish. This phenomenon is a direct consequence of increasing the path length (§3.4 and eq.(13)) .

2.8 Target to clutter power ratio

Figure 6 is an angular amplitude spectrum. While the scatter spectrum is pictured as a smooth continuum, any sample spectrum is itself a random function with peaks and valleys because the spectrum is the Fourier transform of the random phase-screen process. The target can be discerned so long as it well exceeds the peaks of the scatter spectrum. The measure of target detectability is the target contrast or target to clutter power ratio TCR, which can be estimated for a square 2-D array of size L as follows.

The target and the clutter fields spread in two dimensions as they propagate (Figure 7a). Approximate the angular power spectrum by the sum of two right circular cylinders (part b), pictured in cross section as rectangles in part c. The first cylinder is the target spectrum. Its power A^2 spreads over a circle of diameter λ/L. Its height, therefore, is $(AL/\lambda)^2(4/\pi)$. The second spectrum is the clutter region or halo S(u) induced by the target. Its area is $1-A^2$ and its width is $\lambda/\pi x_0$. Its height is $(1-A^2)(\pi x_0/\lambda)^2(4/\pi)$. Hence the target to clutter power ratio within the halo is

$$TCR = \frac{A^2 L^2}{(1-A^2)(\pi x_0)^2} \approx \frac{L^2}{\sigma_\phi^2 (\pi x_0)^2} = \frac{L^2}{\omega^2 \sigma_\tau^2 (\pi x_0)^2} \qquad (11)$$

where the approximation $\Rightarrow A \approx 1$ and $1-A^2 \approx \sigma_\phi^2$. Eq.(11) shows that TCR for a single, thin screen is quadratic with 2-D transducer size (linear with area) and inversely proportional to the

time-delay variance of the screen and the square of the frequency and the correlation distance. The frequency dependence of TCR enters only through $q_\phi^2 = \omega^2 \sigma_\tau^2$, because the density and compressibility variations in the tissue induce time delay variations that are independent of frequency (§2.5).

2.9 Target dynamic range

From TCR (11) we can determine the smallest target that can be detected in the interference background and hence the target dynamic range (TDR), which is the ratio of the largest to the smallest detectable target. Eq. (11) is the ratio of the target intensity to the average intensity of the clutter field within the halo. Because the field develops as a bandlimited, noise-like random process, upward deviations of 10 dB from the mean are not unlikely (order of 1% occurrence frequency)[15]. Hence other targets within the halo that are 10 dB greater than the mean clutter intensity will not be discernible amidst the high peaks in the clutter spectrum. At least a few more dB are required for unambiguous single-look target detection, although with multiple looks 10 dB is sufficient. Thus suitable contrast between the target image and the clutter background within the halo requires a minimum TCR of about 10 dB. In other words, TDR within the halo is about an order of magnitude smaller than TCR.

3. MULTIPLE ADJACENT SCREENS

The input to the first screen is the unit amplitude plane wave shown in Figure 1. The emergent plane wave plus the scattered field (5) is the input to the second screen, the output of which is the input to the third screen, etc., as shown in Figure 8. The emergent radiation is pictured there as angular (Fourier) spectra with the u-axis parallel to each screen.

3.1 Screen thickness and number of screens

The number of screens N is the propagation depth D of a target divided by the screen thickness. The infinitely-thin screen model calls for as small a thickness as other considerations allow. Because of the assumed independence of the phase distribution from screen to screen, screen thickness can be no smaller than scatterer size a. This is also reasonable on physical grounds, for otherwise the scale of the scattering structure would be altered by choice of screen dimension. For these reasons the nominal scatterer size is taken as the lower bound on screen thickness. Thus, for a propagation depth D of 6 cm and a nominal scatter size $a = 1$ cm, the number of screens $N \approx 6$.

3.2 Output angular spectrum

The clutter build-up is illustrated in Figure 8. Its angular spectrum is derived as the output of a cascade of N linear filters, each with angular impulse response $h_n(u)$, $n = 1,2...N$. The first screen has impulse response $h_1(u) = A_1\delta(u) + s_1(u)$, which is the total spectrum out of the first screen. $A_1\delta(u)$ is a Dirac δ-function of amplitude A_1 (power A_1^2) located at the origin in the angular spectrum. $s_1(u)$ is a continuous scatter spectrum of power $1-A_1^2 \approx \sigma_\phi^2$, the phase variance of the screen. The total power is unity, as it must be, because no losses have yet been assumed. The width of $s_1(u)$ is $\Delta u \approx \lambda/\pi x_0$ (9).

Screen 2 has impulse response $h_2(u) = A_2\delta(u) + s_2(u)$. Its angular spectrum is $h_1(u)*h_2(u)$, where * denotes convolution. It consists of three parts; a plane wave of amplitude A_1A_2, the sum of two primary scatter spectra, $A_2s_1(u) + A_1s_2(u)$, and a secondary scatter field $s_1(u) * s_2(u)$. The first primary scatter spectrum arises from the $s_1(u)$ passing unchanged in shape through the screen but reduced in amplitude by A_2, the plane-wave voltage gain of screen 2; the second is the scattering $A_1s_2(u)$ of the plane wave incident upon screen 2. The power in the primary scatter spectrum is $A_2^2(1-A_1^2) + A_1^2(1-A_2^2)$. The power in the second order scatter spectrum is $(1-A_1^2)(1-A_2^2)$. The total power in the emergent field is again unity $(A_1^2A_2^2 + A_2^2[1-A_1^2] + A_1^2[1-A_2^2] + [1-A_1^2][1-A_2^2] = 1)$.

The angular spectrum from screen 3 it is $h_1(u)*h_2(u)*h_3(u)$. It consists of a plane wave $A_1A_2A_3\delta(u)$, a primary scatter field $A_3[A_2s_1(u) + A_1s_2(u)] + A_1A_2s_3(u)$, a secondary field $[A_2s_1(u) + A_1s_2(u)] * s_3(u) + A_3[s_1(u) * s_2(u)]$ and a tertiary scatter field $s_1(u) * s_2(u) * s_3(u)$. The primary scatter power is $A_3^2A_2^2(1-A_1^2) + A_3^2A_1^2(1-A_2^2) + A_1^2A_2^2(1-A_3^2)$. The secondary scatter power is $A_2^2(1-A_1^2)(1-A_3^2) + A_1^2(1-A_2^2)(1-A_3^2) + A_3^2(1-A_2^2)(1-A_1^2)$ and the tertiary scatter power is $(1-A_1^2)(1-A_2^2)(1-A_3^2)$.

After N screens the angular spectrum is the N-fold convolution $h_1(u)*h_2(u)*\cdots*h_N(u)$. It contains a δ-function representing the emergent plane wave. Its amplitude is $A_1A_2\cdots A_N$ which we will call A^N, where A is the geometric mean of the A_i. This is the target. All other components of the output spectrum add to create the signal-induced clutter spectrum.

The power spectrum of the output primary clutter field in Figure 8 is the sum of the primary power spectra and similarly for the higher order scattered fields. Fortunately this complicated picture can be simplified considerably.

3.3 Output power spectra

Schema of cross sections of the target spectrum and the first three scatter spectra are illustrated in Figure 9. The output target power $P_T = [\prod_{i=1}^{N} A_i]^2 = A^{2N}$. The target power is spread in both dimensions over the diffraction pattern of the transducer. The bulk of the power is in the main lobe. Its beamwidth is λ/L and its angular cross section is $(\pi/4)(\lambda/L)^2$. Within the

beam the power density is $\dfrac{4A^{2N}}{\pi(\lambda/L)^2}$. Its spectrum is shown schematically in the upper part of Figure 9.

The $s_i(u)$ are independent spectra because they are derived from independent sample functions of the random phase-delay process defining the inhomogeneous medium. They are continuous, noise-like terms with zero means and their powers add. The same is true for convolutional terms such as $s_i(u) * s_j(u)$, $s_i(u) * s_j(u) * s_k(u)$, etc. What is pertinent for each such term is its width and its power and to a much lesser extent its shape. All $s_i(u)$ have the same nominal width, power and shape. Therefore we identify all $s_i(u)$ with a generic first order random scatter spectrum $s(u)$, all $s_i(u) * s_j(u)$ with a generic second order scatter spectrum $s(u) * s(u)$, and so forth. The half-power width of $s(u)$ is $\lambda/\pi x_0$. Variances add under convolution. Therefore the width of $s(u) * s(u)$ is $\sqrt{2}\lambda/\pi x_0$. The widths of higher order convolutions are $\sqrt{3}\lambda/\pi x_0$, $\sqrt{4}\lambda/\pi x_0$, etc. Areas multiply under convolution. The power in $s(u)$ is $1-A^2$, in $s(u) * s(u)$ it is $(1-A^2)^2$, etc. One $s(u)$ term arises from the first screen, two $s(u)$ terms weighted by A from the second, three $A^2 s(u)$ terms from the third, and so forth. Finally, N $s(u)$ terms emerge from the final screen with a weight of A^{N-1}. The power in each term is $(1-A^2)A^{2(N-1)}$. Because the N $s(u)$ terms are independent, their powers add. Therefore the power in the first order scatter spectrum $P_{C1} = N(1-A^2)A^{2(N-1)}$.

Similarly the power in the second order spectrum $P_{C2} = \binom{N}{2}(1-A^2)^2 A^{2(N-2)}$. $P_{C2} << P_{C1}$ because A must be close to unity to achieve adequate TCR for useful imaging. For the third order $P_{C3} = \binom{N}{3}(1-A^2)^3 A^{2(N-3)} << P_{C2}$, and so on.

The power density is estimated in the same way as was done for the target. The power in the first order scatter field P_{C1} is spread over the scattering angle of $s(u)$, which is $\lambda/\pi x_0$, within which the power density is $P_{C1}/(\lambda/\pi x_0)^2(\pi/4)$, and similarly for the higher order scatter fields. The power in each successive scatter order decreases by the factor $(1-A^2)$. Because A is close to unity, this ensures that the first order scatter field dominates.

3.4 Target to clutter power ratio

Combining the terms above, the target to clutter power ratio for N screens is

$$TCR = \frac{L^2 A^{2N}}{(\pi x_0)^2 \sum\limits_{n=1}^{N} \binom{N}{n}\left(1-A^2\right)^n A^{2(N-n)}} \qquad (12)$$

Eq.12 can be simplified considerably. Figure 10 plots TCR vs. $\sigma_\phi^2 \approx 1-A^2$ within the "clutter" region for $L = 25$ mm, $\pi x_0 = 10$ mm and $N = 6$, the number used in the earlier example. The minimum useful TCR must be larger than 10 dB because the target dynamic range is about 10 dB smaller than TCR ($\S2.9$). Thus the maximum phase variance per screen is about 0.01 sq rad for unambiguous detection. Thus, only very small phase variance per screen can be tolerated for otherwise the target rapidly gets lost in the background as σ_ϕ^2 grows. Therefore we can assume $\sigma_\phi^2 \approx 10^{-2}$ and $A^2 \approx 1 - \sigma_\phi{}^2$. Next, $Na \approx D$ and $a \approx \pi x_0$. Also $\sigma_\phi{}^2 = \omega^2 \sigma_\tau{}^2$. Therefore (12) becomes

$$TCR \approx \frac{L^2}{(\pi x_o)^2 \sum\limits_{n=1}^{N} \binom{N}{n}\left(\frac{\sigma_\phi^2}{A^2}\right)^n} = \frac{L^2}{(\pi x_o)^2\left(\left(\frac{\sigma_\phi^2}{A^2}\right)-1\right)^N}$$

$$\approx \frac{L^2}{(\pi x_o)^2 N \sigma_\phi^2} \approx \frac{L^2}{\pi x_o D \omega^2 \sigma_\tau^2}$$

(13)

Not surprisingly (13) has the same form as (11), the single screen TCR, because of the dominance of the primary scatter field. In essence both are weak scattering solutions.

Eq.13 predicts that TCR is inversely proportional to propagation distance. 9 *in vitro* TCR measurements were made at the Univ. of Rochester laboratory of Prof. Robert Waag from five samples of different thicknesses of excised, frozen and defrosted breast tissue used in Ref.10. For each measurement, a tissue sample was fixed in a holder within a water tank. Propagation was one-way from a pulsed 3.75 MHz hemispherical (virtual point-) source, through the water and tissue path, to a 1-D linear array in which waveforms were recorded at each element. The array was mounted in a computer-controlled 2-D positioner and moved along the orthogonal axis so as to form a 92x46 sq mm, 2-D synthetic array. Waveforms measured at each element position of the synthetic 2-D array were imaged. Figure 11 shows a 1-D maximum-projection cut through such an image. TCR measurements were made from such cuts. The central lobe is the image of the source. Clustered around it are discrete multipath arrivals from the source. They image as false targets. The broad clutter background is the isotropic scatter field. TCR is the squared reciprocal of the estimated clutter level at the origin. The 9 TCR data points are shown on the log-log plot of Figure 12a. Each point is the average of measurements made from a minimum of 6 cuts. The straight line drawn in the figure has the predicted slope of -1. With the exception of one point - the outlier at 30 mm depth - the data approximate the predicted behavior.

3.5 Relations between single and multiple screen parameters

Correlation distance: A significant amount of multiple scattering is precluded because σ_ϕ^2 has to be small ($\sim 10^{-2}$ sq rad) for successful imaging. This dominance of the primary scatter field means that the spectral width does not increase with propagation path length. Consequently, x_0 is a function of scatterer size only and not the thickness of the propagation medium in which it is measured. Experimental data support this conclusion. Measured halo widths from different thicknesses of a single *in vitro* breast sample used in Ref.10 are plotted in Figure 12b. The angular width is constant over a thickness range from 15 to 40 mm. Thus correlation measurements made in a given type of tissue at one depth are pertinent for any other depth.

Phase variance: σ_ϕ^2 in (13) is the phase variance of a single screen. A measurement in tissue, however, is never across a single screen and therefore the relation of measured phase variance data to σ_ϕ^2 must be determined. We can view the sequence of screens in the multi-screen model as a cascade of linear filters each with phase delay $\phi_i(x)$ or time delay $\tau_i(x)$. The phase (and time) delays add across a group of such circuits. Thus a phase measurement across N screens yields $\phi_1(x)+\phi_2(x)+\phi_3(x)+... = \sum_{i=1}^{N} \phi_i(x)$ and because of the assumed independence and common statistics of the $\phi_i(x)$ the variance is $N\sigma_\phi^2$, which accounts for the factor of N in (13).

3.6 Absorption

To incorporate absorption in the model, an exponential loss $\exp(-\alpha z)$ is appended such that the total field through each screen of thickness a is attenuated by the factor $\exp(-\alpha a)$ where α is assumed independent of positiion. The gain of the ith screen to the plane-wave component of the field changes from A_i to $A_i' = A_i\exp(-\alpha a)$. Output target power $P_T = [\prod_{i=1}^{N} A_i]^2 = A^{2N}$ (§3.3) changes to $[\prod_{i=1}^{N} A_i']^2$

$= A^{2N}\exp(-2N\alpha a)$.

The clutter is modified similarly. All scatter field terms in §3.2, calculated for a lossless model, are attenuated by the factor $\exp(-\alpha a)$. The first order spectrum $P_{C1} = N(1-A^2)A^{2(N-1)}$ changes to $N(1-A^2)e^{-2\alpha a}A^{2(N-1)}e^{-2(N-1)\alpha a} = N(1-A^2)A^{2(N-1)}e^{-2N\alpha a}$. Target to clutter ratio remains unchanged for the primary scatter spectrum, and similarly for the higher order spectra.

The same is true for the ratio P_{scat}/P_{pw}; absorption does not affect the balance between the scattered and plane wave components. Further, the argument holds at every frequency and therefore frequency selective absorption, which alters the spectrum of a deeply propagating wideband pulse, does not affect the ratio of the scattered to the plane wave energy.

Also unaffected by absorption are the relative strengths of the components of the scattered field that arise from different depths. This is because all components, whether plane wave or scattered field, are attenuated identically by the time they reach the skin. To illustrate this phenomenon, consider primary scattering arising from the nth screen, which means at a

depth of na. The plane wave component that initiates this field is attenuated by absorption, as it travels through n-1 screens toward the skin surface, by the factor $A^{2(n-1)}e^{-2\alpha a(n-1)}$. In the nth screen the scattered field $s(u)$ is attenuated by the factor $e^{-2\alpha a}$. As this field propagates to the skin surface it suffers additional attenuation in the remaining N-n layers by the factor $A^{2(N-n)}e^{-2(N-n)\alpha a}$. The emergent scattered field is the product $\{A^{2(n-1)}e^{-2\alpha a(n-1)}\}\{s(u)e^{-2\alpha a}\}\{A^{2(N-n)}e^{-2(N-n)\alpha a}\} = A^{2(n-1+N-n)}e^{-2\alpha a(n-1+1+N-n)}s(u) = A^{2(N-1)}e^{-2N\alpha a}s(u)$, which is independent of n. In other words all scattered fields arising from the same target reach the surface with the same strength. Consequently the scattered field measured at the surface is a composite of the scattering all along the path from target to surface.

3.7 Parameters obtained from measurements

Finally, we rewrite (13) in terms of measurable parameters. Assume that measurements of correlation distance and time delay variance are made across a body of length $D_m \gg a$, where a is the nominal thickness of a phase screen. Call the measurements x_{0m} and $\sigma_{\tau m}^2$. The parameters needed for analysis are the single-screen values x_0 and σ_ϕ^2 or σ_τ^2. Both can be obtained from the measured data. As discussed above (§3.5) $x_0 = x_{0m}$ because of the dominance of primary scattering. The single screen phase variance σ_ϕ^2 is calculated from $\sigma_\phi^2 = \sigma_{\phi m}^2/N_m$, as shown in §3.5, and $\sigma_\phi^2 = \omega^2\sigma_\tau^2$. N_m is the number of screens or scatterer sizes a in D_m. $\therefore \sigma_\phi^2 \approx a\sigma_{\phi m}^2/D_m$ is the single screen phase variance. Eq.(13) can then be rewritten as a function of the known parameters of the imaging system (ω, L), the propagation depth during imaging (D), the measured tissue parameters (x_{0m}, $\sigma_{\phi m}^2$ or $\sigma_{\tau m}^2$) and the propagation depth during measurement (D_m):

$$TCR \approx \frac{L^2}{N\sigma_\phi^2(\pi x_0)^2} \approx \frac{L^2}{D(\pi x_0)^2(\sigma_{\phi m}^2/D_m)} \approx \frac{L^2}{D\omega^2(\pi x_{0m})^2(\sigma_{\tau m}^2/D_m)} \qquad (14)$$

where the last approximation uses $a = \pi x_{0m}$ and $\sigma_{\phi m}^2 = \omega^2\sigma_{\tau m}^2$. The right-hand expression is the most generally useful form.

The numerator parameter and first two denominator parameters are design parameters. The next two denominator parameters are measured properties of the tissue. The last is the length of the tissue sample in which tissue parameter measurements are made. Thus, time delay variance and correlation distance are the primary tissue measurements required for prediction of TCR in a purely scattering medium.

3.8 Limit to resolution

In §2.7, the lateral resolution was found to remain λ/L, the width of the diffraction pattern, and unaffected by the scatter field *so long as the scattered energy does not obscure the*

main image lobe. When detection vanishes so do lateral and contrast resolution, as was observed in 12-cm path-length observations reported in Refs.7 and 8.

4. OTHER RELATED TOPICS

4.1 Near field

The theoretical development of the scatter field used a plane wave or far-field model whereas ultrasonic imaging instruments are focused in the near field. There are two separate matters here. First, the physics of scattering has nothing to do with the focal properties of the measuring instrument and hence is unrelated to whether or not the instrument is focused. Second, the scatter spectrum from which spectral width was calculated extends only a few beamwidths from the focus and hence is satisfactorily approximated by the far-field Fourier transform calculation of the scattered field in (1). Thus the plane wave model is acceptable.

4.2 Two-way propagation

The model deals with both point source radiation propagating one-way to a receiving array and to the two-way problem of an isolated point target when illuminated by an arbitrary transmitter. It does not cover the arbitrary target distribution with arbitrary insonification. In principle the method can be extended to any source/target/transmitter configuration and in this paper two practical and easily describable cases are given.

One case is the well-focused transmitter. Only the target is illuminated with full strength. All other targets receive sidelobe illumination. Therefore the scatter level from the target is higher than the other scattered fields by the sidelobe level of the transmitter. Those fields are not first order competitors to the primary scatter background from the target and in general can be ignored.

In another important case the transmitter focus is degraded by the inhomogeneous medium from λ/L to $\lambda/\pi x_0$, the width of the primary clutter spectrum, where $L >> x_0$. Now all targets within a 2-D circle of diameter $\lambda/\pi x_0$ are illuminated nearly equally and contribute equally to the clutter background. For the sake of argument, let there be $L/\pi x_0$ targets per diameter (one per beamwidth) of nominally the same size (such as Rayleigh scatterers) so insonified. Then the number of illuminated scatterers in a circle of diameter $L/\pi x_0$, which is $(\pi/4)(L/\pi x_0)^2$, is the factor by which the clutter power increases. The total received clutter power is spread in two dimensions over roughly twice the area (diameter is $\sqrt{2}\lambda/\pi x_0$ because the received spectrum, being the convolution of the scatter-source spectrum on transmit and the medium-induced spectrum on receive, is $\sqrt{2}$ times larger in diameter). The result is a change in TCR by the factor $(8/\pi)(\pi x_0/L)^2$.

A more general case is an arbitrary target distribution T(u) illuminated by a field f(u) from a transmitter radiating through an inhomogeneous medium. Its scatter field is T(u)f(u)∗s(u), the convolution of the medium response to the target reradiation. Further, let the target distribution be discrete and described by $T(u) = \Sigma T_k \delta(u-u_k)$ where the T_k are the amplitudes of targets located at $u=u_k$. The scatter field is $s(u)\ast f(u)\Sigma T_k \delta(u-u_k) = s(u)\ast \Sigma T_k f_k \delta(u-u_k) = \Sigma T_k f_k s(u-u_k)$ where $f_k = f(u-u_k)$.

4.3 Limitations of the model

Infinite statistically homogeneous phase screen: This model of spatially stationary statistics is satisfactory for weak scattering in a single, large tissue bed. It fails to account for interfaces between tissue beds across which a sound velocity change takes place. In other words, the model ignores all multiple angular arrivals at the transducer array from a common source which could arise from refraction at an interface or reflection from a strongly reflecting surface. Such arrival wavefronts will interfere in the aperture and appear to the imaging system as multiple sources, each with its own scattering halo.

The model is expected to be realistic in a large, reasonably homogeneous organ such as liver and for the purely scattering component in breast from subcutaneous and intramammary fat that fill much of most breasts. High density tumors and liquid-filled cysts will refract wavefronts and introduce image artifacts. It is hoped that these will submit to modeling at a later time.

Array size: The model is appropriate for arrays that are not too small to perceive the spatial fluctuations in $\phi(x)$, for then a statistical description of the medium is inappropriate, nor so large as to violate spatial stationarity (fluctuation statistics no longer constant across the array). The smaller limit likely occurs when $L \ll a$. In the other extreme the array not only sees a stochastic field of random spatial-density fluctuations but also discrete sub-bodies (cysts, tumors) with different refractive indices. In this case the model given in this paper pertains only to the purely scattered portion of the field, to which it can be applied, but not to the coherent multipath from the discrete bodies.

5. SUMMARY AND OBSERVATIONS

Inhomogeneous tissue removes energy from a wave both by incoherent scattering and coherent refraction and reflection. The incoherent scattered field is studied in this paper. The modeling technique is to slice the tissue body into thin, random phase screens, calculate the properties per screen and combine them. Scattering is produced by random speed fluctuations in tissue, largely due to density and compressibility perturbations. The nominal distance between density hills is identified with scatterer size $a \approx \pi x_0$, where x_0 is the exponential correlation distance. Scattering creates a halo around the target that diminishes the image

contrast. The halo width is $\approx \lambda/a$. The loss in contrast is measured by the target to clutter power ratio, which diminishes with the correlation distance, the propagation length D in the tissue and the time-delay variance per unit distance, and the square of the frequency. Lateral resolution within the halo is unaffected by the scatter field; it remains λ/L. L is the array size. However, detection of weak targets within the halo of a strong target requires that TCR $>>1$. When TCR is small, however, detection is not possible and the preservation of the lateral resolution is a meaningless virtue.

The obscuring effect of the halo is not only from its intensity but also from the number of lateral resolution cells in which the clutter can hide targets. This number is the ratio of the halo cross section to the beam cross section, which is $(L/a)^2$. This ratio is independent of wavelength. Scattering occurs at all depths between target and skin surface. The principal scattering mechanism is single or first-order scattering because the energy removed by each scattering hill is small.

The following summarizes comparisons between predictions of the theory and experimental data.

1. Halo width: Based on the size of fat globules the theory predicts 2-6 deg at 3 MHz (§2.4). Calculations from wavefront correlation experiments give the same spectral width (§2.3).

2. e^{-1} correlation distance vs. frequency: The experiment shown in Figure 3 indicates independence, which is what the theory predicts (§2.5).

3. TCR vs. propagation depth: Theory predicts inverse linear dependence. Experiment shown in Figure 12a indicates approximately the same behavior.

4. Halo width vs. propagation depth: Theory predicts independence. Experiments show the same (Figure 12b).

REFERENCES

1. R.A.Muller and A.Buffington, "Real-Time Correction of Atmospherically Degraded Telescope Images through Image Sharpening," J.Opt. Soc. Am., 64(9) 1200-1210 (September 1974).

2. J.P.Hamaker, J.D.Sullivan and J.E.Noordam, "Image Sharpness, Fourier Optics, and Redundant-Spacing Interferometry," J. Opt. Soc.Am., 67(8) 1122-1123 (August 1977).

3. M.O'Donnell and S.W. Flax, "Phase Aberration Correction using Signals from Point Reflectors and Diffuse Scatterers: Measurements," IEEE Trans. Ultrason. Ferroelec. Freq. Cont., 35(6):768-774, Nov. 1988.

4. L. Nock, G.E. Trahey, S.W. Smith, "Phase Aberration Correction in Medical Ultrasound Using Speckle Brightness as a Quality Factor," J. Acoust. Soc. Am., 85(5) 1819-1833 (1989).

5. C.Prada, F.Wu and M.Fink , "The iterative time reversal mirror: A solution to self-focusing in the pulse mode," J.Acoust.Soc.Am. 90(2), Pt.1, pp. 1119-1129, Aug.1991.

6. Sumino, Y. and Waag, R. C., "Measurements of Ultrasonic Pulse Arrival Time Differences Produced by Abdominal Wall Specimens," J. Acoust. Soc. Am. 90(6) 2924-2930 (1991).

7. Q. Zhu and B.D.Steinberg, "Large-Transducer Measurements of Wavefront Distortion in the Female Breast," Ultrasonic Imaging, 14: 276-299 (1992).

8. Zhu, Q., Steinberg, B. D.and Arenson R., "Wavefront Amplitude Distortion and Image Sidelobe Levels - Part II: In Vivo Experiments", IEEE Trans. Ultrason. Ferroelec. Freq. Cont.40(6) 754-762 (Nov. 1993).

9. Q. Zhu and B. D. Steinberg, "Modeling, Measurement and Correction of Wavefront Distortion produced by Breast Specimens," IEEE Int'l Symp. Ultrason. Ferroelec. Freq. Cont., Cannes, Nov. 1994.

10. L. M. Hinkelman, D-L. Liu, Q. Zhu, B.D. Steinberg, and R. C. Waag, "Measurement and Correction of Ultrasonic Pulse Distortion Produced by the Human Breast", JASA, in press.

11. B.D.Steinberg, *Principles of Antenna and Array System Design*, John Wiley and Sons, New York, 1976.

12. Zhu, Q. and Steinberg, B. D., "In vivo measurement of correlation length of female breast," submitted to JASA Nov. 92, accepted subject to revision.

13. A.Castro and R.Gomberg, *Le Sein: Mammographie. Echographie. Numerization. Galactographie*, Arnette, 2 rue Casimir Delavigne, 75006 Paris, 1989.

14. B.D.Steinberg and Q.Zhu, "Lateral Resolution in the Breast as a Function of Transducer Size," UP-VFRC-22-92, Valley Forge Res. Cntr., UPenn., Phila. PA, 1992.

15. Any text on statistical communications or radar theory, e.g., M. Schwartz, *Information Transmission. Modulation and Noise*, McGraw Hill, New York, 1970.

16. B.D.Steinberg, "Radar imaging from a distorted array: The radio camera algorithm and experiments," IEEE Trans. Ant. Propag., AP-29(5), 740-748 (Sept. 1981)
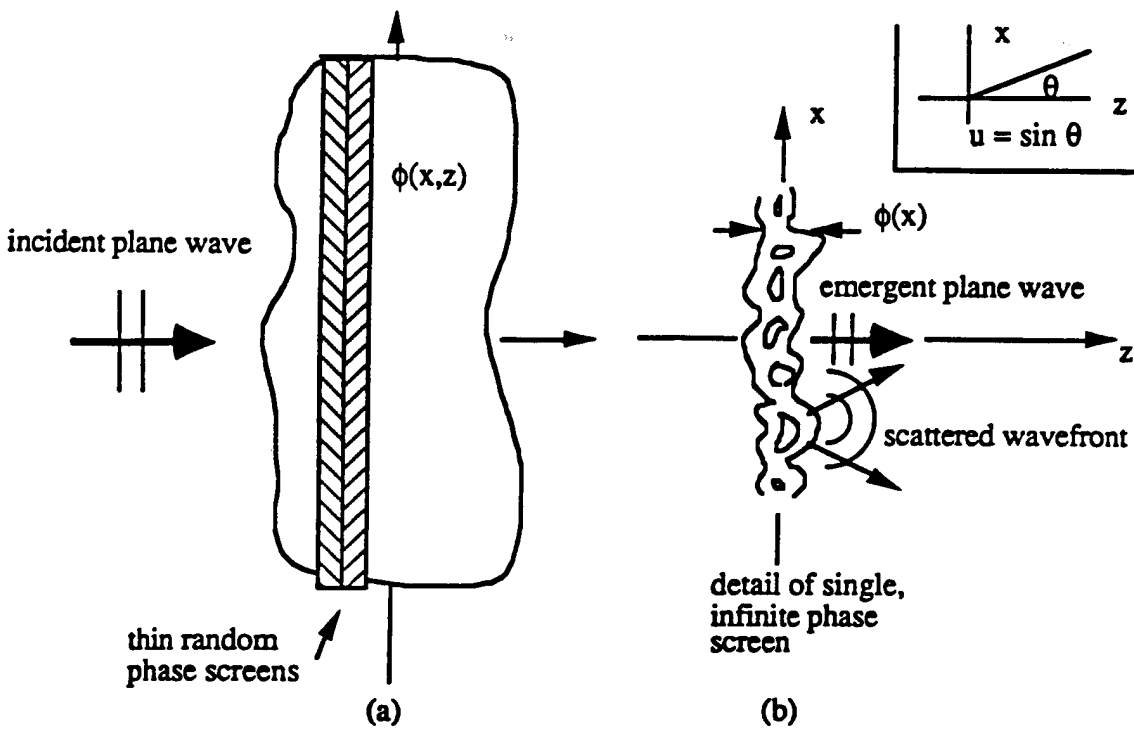
Figure 1. (a) Random, statistically homogeneous medium modeled as sequence of adjacent random phase screens. (b) Detail of single, infinite screen showing density variations (contours) as cause of local perturbations of time delay through screen. Some of the energy of the plane wave incident upon the screen emerges as a plane wave. The remainder is scattered. Shown is the scattered wavefront from one scattering center in the screen.
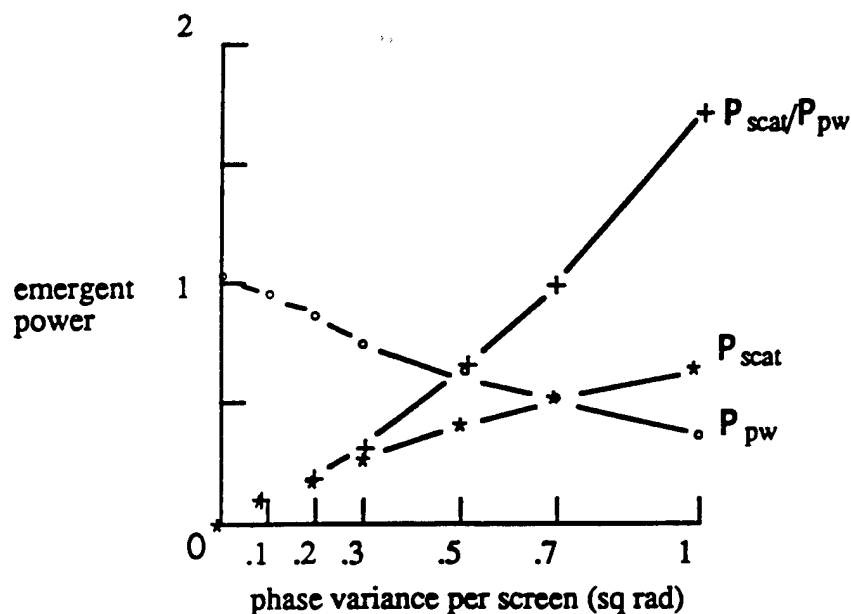
Figure 2. Emergent energy vs phase variance $\sigma_\phi^2 = (2pfs_t)^2$. Single phase screen. $P_{pw} = A^2$ = plane wave power, $P_{scat} = 1-A^2$ = scattered power, P_{scat}/P_{pw} = ratio of scattered to plane wave powers.

(a)   (b)
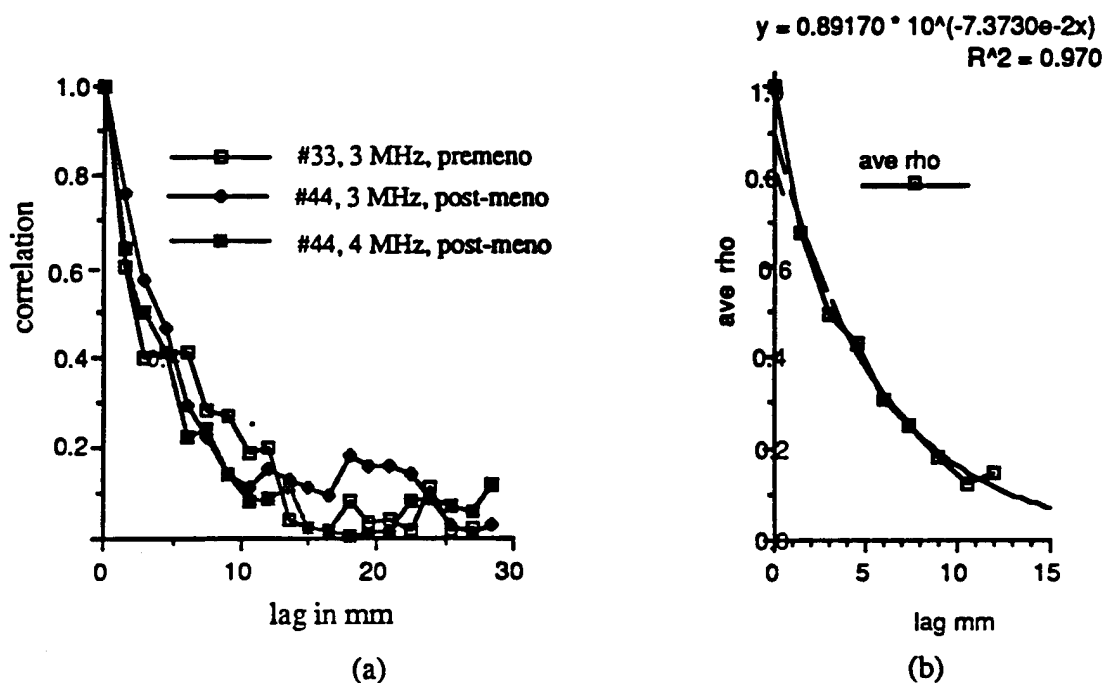
Figure 3. (a) Point source correlation functions of 12-cm thickness *in vivo* breasts measured 2.5-3 cm from chest wall. Data from Ref 1. (b) Average of the three curves of (a) and exponential fit.

Ganglion

Muscle
pectoral

Crête de
Duret

Peau

Tissu graisseux
sous-cutané

Lobule

Galactophore

Bourse graisseuse
rétromammaire

Aréole

Mamelon

Sinus galactophorique
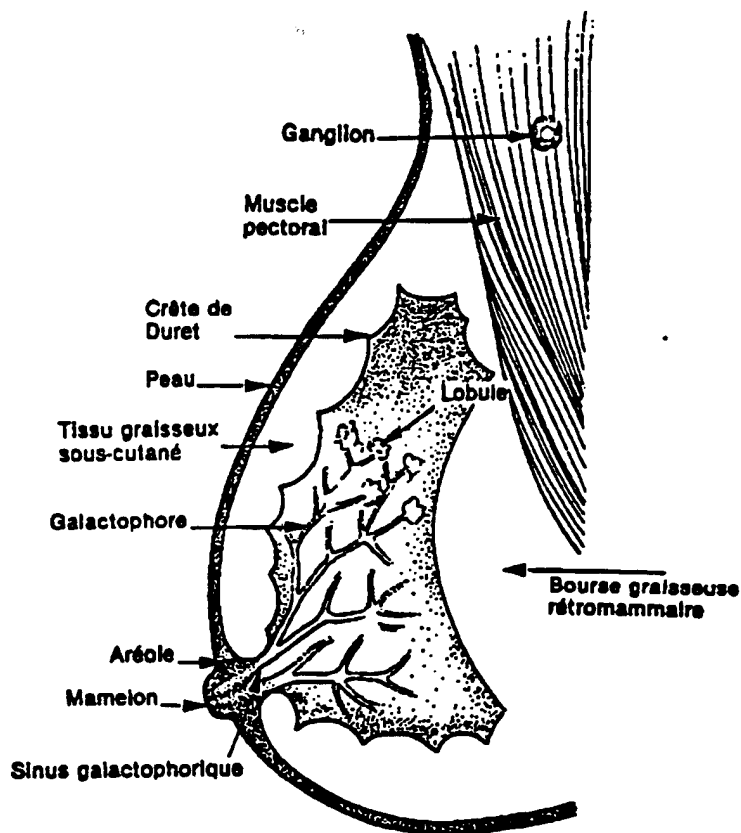
Figure 4. Schematic of breast section. From Ref. 13.

1

$\dfrac{\lambda}{\pi x_0}$

A

L

screen

lens, transducer, etc.

image of target is
diffraction pattern
of aperture

λ / L

scatter spectrum

$\approx \lambda / \pi x_0$

focal plane
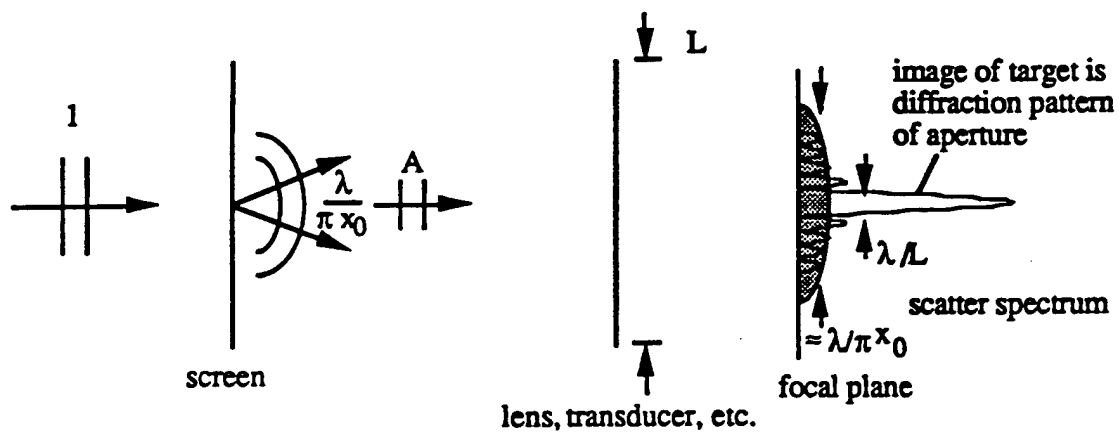
Figure 5. Image contains diffraction pattern of aperture (image of emergent plane wave) and angular spectrum of the scatter field.
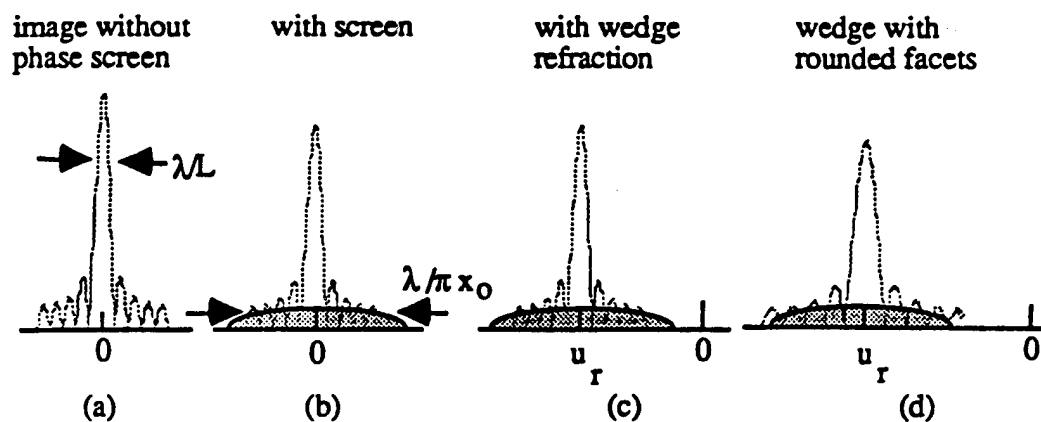
Figure 6. Image of point source is diffraction pattern of imaging aperture. (a) Without phase screen. (b) Scatter spectrum caused by phase screen. Image power reduced. (c) Linear-wedge refraction plus weak scattering. Image displaced through angle u_r. (d) Wedge with rounded facets defocuses image.
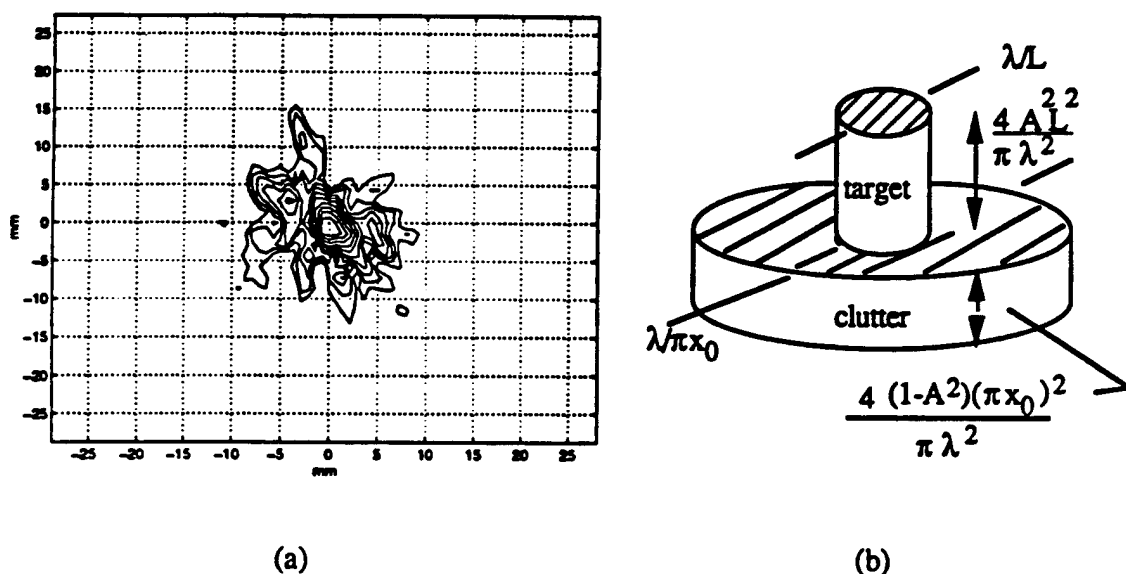
Figure 7. Angular target and clutter spectra. (a) Contour plot of point target (center contours) plus widely dispersed scattered field and discrete multipath. The coordinates are azimuth and elevation. *In vitro* breast sample (brs006) is 4-cm thick. 3.75 MHz. 92 mm x 46 mm array. Outer contour -15 dB. Data from experiment reported in Ref. 10. (b) Approximate target and clutter spectra showing heights and widths.

50
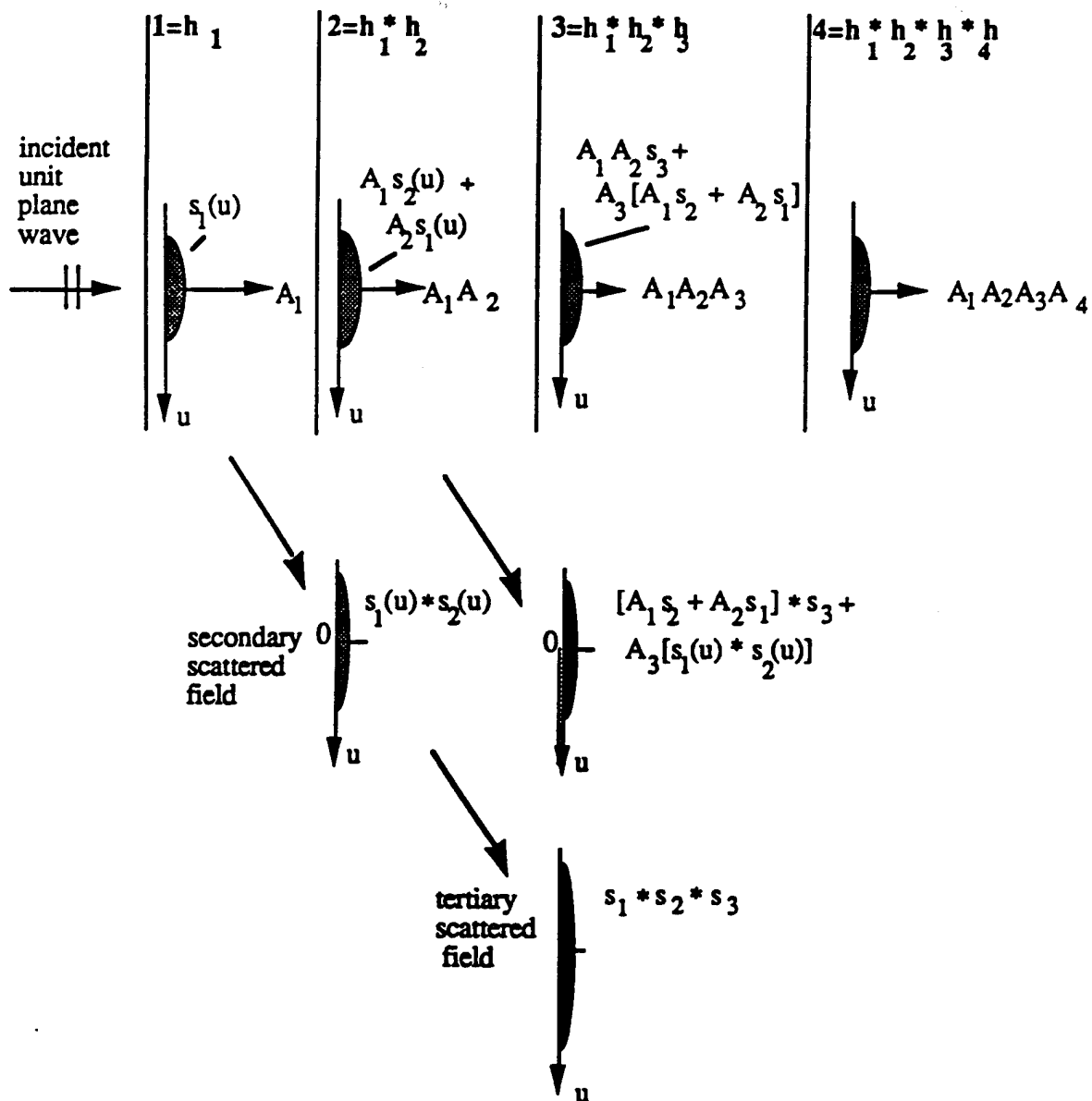
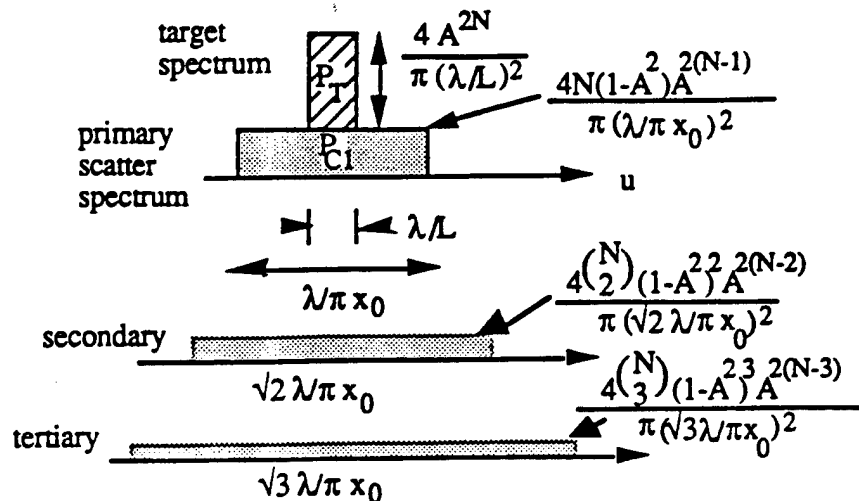Figure 8. Build-up of the multiple-screen angular output spectrum.

Figure 9. Cross sections of approximate target and clutter spectra after N screens. 2-D array.
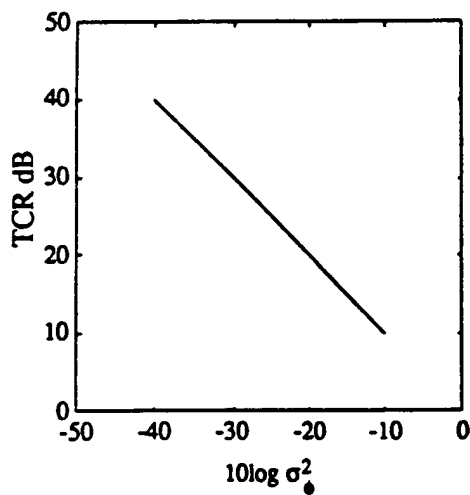

Figure 10. Ratio of point target intensity in image to clutter background induced by scattering. σ_ϕ^2 is the phase variance per screen. 6 screens, 25 mm array size, 10 mm scatterer size. Plot of (13).
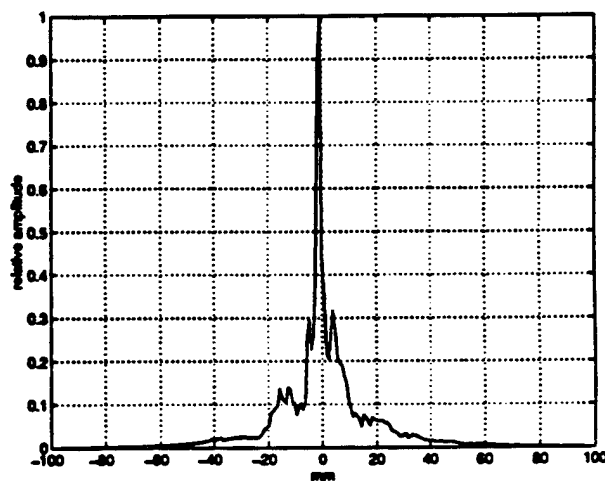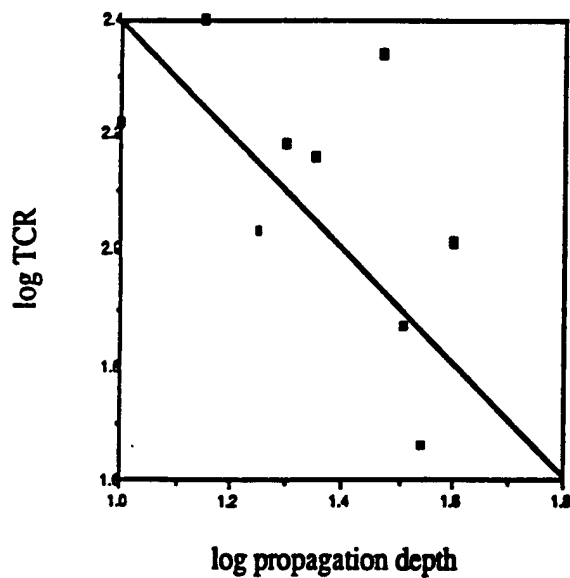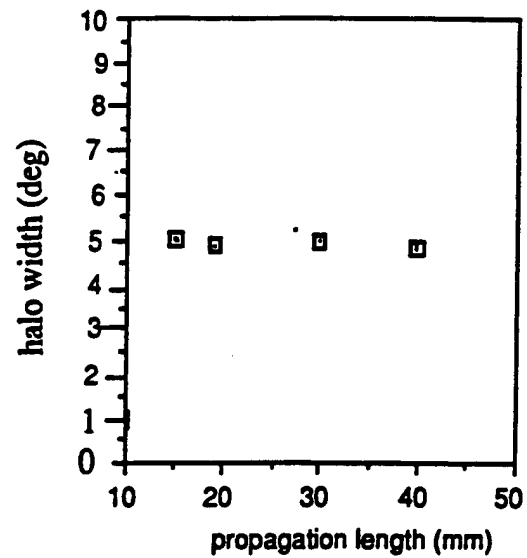
Figure 11. 1-D cut at -25 deg through single-source image of Figure 7a. System noise level $\approx$ -35 dB. Cut is through region with minimum multiple arrivals. Central lobe is target image. Adjacent lobes are multipath, probably refraction induced. Low, broad background is isotropic scattering. TCR and halo width are estimated from the scatter background.

(a)

(b)

Figure 12. (a) TCR and (b) halo width (deg) vs. thickness of *in vitro* breast samples. TCR shows approximate inverse linear dependence (solid line) with path length. Halo width shows independence.